Supplementary Information (SI) for Journal of Materials Chemistry A.

Revealing a Synergistic Orbital Coupling Adsorption Mechanism of Oxygen Reduction Reaction in Dual-Atom Catalysts

Yangfan Liu,[1] Yejun Li,[1,2*] Xinghan Liu,[2] Jinming Li,[2] Gufei Zhang,[3,4] Jun Gong,[5]
Yanbin Jiang,[1*] Zhou Li[1*]

[1] School of Materials Science and Engineering, Central South University, 410083 Changsha, P.R. China

[2] Hunan Key Laboratory of Nanophotonics and Devices, School of Physics, Central South University, 410083 Changsha, P.R. China

[3] National Key Laboratory of Science and Technology on Advanced Composites in Special Environments, Harbin Institute of Technology, 150080 Harbin, P.R. China

[4] Zhengzhou Research Institute, Harbin Institute of Technology, 450000 Zhengzhou, P.R. China

[5] School of Mechanical Engineering, Hunan University of Science and Technology, 411201 Xiangtan, P.R. China

[*]Email: yejunli@csu.edu.cn; jiangyanbin@tsinghua.org.cn; lizhou6931@csu.edu.cn

Details of the DFT calculation section:

ORR path in acidic media:

$$* + O_2 \rightarrow *O_2 \qquad (1)$$

$$*O_2 + H^+ + e^- \rightarrow *OOH \qquad (2)$$

$$*OOH + H^+ + e^- \rightarrow *O + H_2O \qquad (3)$$

$$*O + H^+ + e^- \rightarrow *OH \qquad (4)$$

$$*OH + H^+ + e^- \rightarrow * + H_2O \qquad (5)$$

where * denotes the active site on Slab (the pure M_1M_2-NDG), and $*O_2$ (M_1M_2-NDG&O_2), *OOH (M_1M_2-NDG&OOH), *O (M_1M_2-NDG&O), *OH (M_1M_2-NDG&OH) denote the intermediates formed when O_2, OOH, O, OH adsorb on the Slab, respectively.

For free energy calculations, we used the computational hydrogen electrode (CHE) model developed by Nørskov et al.[1] (Expresses the chemical potential of H^+ and e^- in terms of the free energy of $1/2H_2$, i.e., $H^+ + e^- = 1/2H_2$), with the following reaction equation:

$$\Delta G = \Delta E + \Delta ZPE - T\Delta S - \Delta G_U - \Delta G_{pH} \qquad (6)$$

ΔE, ΔZPE, and ΔS denote the difference between the formation energy, zero-point energy, and entropy of the reactants and products, respectively. T denotes the temperature, which is set to 298.15 K. $\Delta G_U = -neU$, where U is the applied potential of the electrode, e is the elementary charge, and n is the number of electrons transferred. $\Delta G_{pH} = K_BT \times \ln10 \times pH$, where K_B is Boltzmann's constant, and considering that the electrochemical reaction occurs in an acidic medium environment, the pH value is set to 0 in this paper, i.e. $\Delta G_{pH} = 0$.

The corresponding reaction energy barriers (ΔG_n, n = 1~5) are calculated with the following equations:

$$\Delta G_1 = G_{*O_2} - G_{Slab} - G_{O_2} \tag{7}$$

$$\Delta G_2 = G_{*OOH} - G_{*O_2} - 1/2G_{H_2} \tag{8}$$

$$\Delta G_3 = G_{*O} + G_{H_2O} - G_{*OOH} - 1/2G_{H_2} \tag{9}$$

$$\Delta G_4 = G_{*OH} - G_{*O} - 1/2G_{H_2} \tag{10}$$

$$\Delta G_5 = G_{*} + G_{H_2O} - 1/2G_{H_2} \tag{11}$$

where G_*, G_{*O_2}, G_{*OOH}, G_{*O}, G_{*OH} denote the free energy of Slab, $*O_2$, *OOH, *O, *OH, and G_{H_2}, G_{O_2}, G_{H_2O} denote the free energy of H_2, O_2, H_2O, respectively. Moreover, for the different reaction paths present in the heteronuclear DACs system and the corresponding reaction energy barriers, one can refer to the **Fig. S1** and **Note S1**.

The overpotential ($\eta_{ORR,\ DFT}$) expression is as follows (U = 1.23 V):

$$\eta_{ORR,\ DFT} = \max\{\Delta G_1, \Delta G_2, \Delta G_3, \Delta G_4, \Delta G_5\}/e \tag{12}$$

The equations for the binding ($E_{b1\text{-}M_1/M_2}$) and dissociation energy ($U_{diss1\text{-}M_1/M_2}$) of M_1/M_2-NDG are as follows:

$$E_{b1\text{-}M_1/M_2} = E_{M_1/M_2\text{-}NDG} - E_{M_1/M_2} - E_{NDG} \tag{13}$$

$$U_{diss1\text{-}M_1/M_2} = U_{M_1/M_2} - E_{b1\text{-}M_1/M_2}/ne \tag{14}$$

The equations for the binding ($E_{b2\text{-}M_1/M_2}$) and dissociation energy ($U_{diss2\text{-}M_2/M_1}$) of M_1M_2-NDG are as follows:

$$E_{b2\text{-}M_1/M_2} = E_{M_1M_2\text{-}NDG} - E_{M_2/M_1} - E_{M_1/M_2\text{-}NDG} \tag{15}$$

$$U_{diss2\text{-}M_2/M_1} = U_{M_2/M_1} - E_{b1\text{-}M_2/M_1}/ne \tag{16}$$

where $E_{M_1/M_2\text{-NDG}}$ and $E_{M_1M_2\text{-NDG}}$ denote the formation energy of M_1/M_2-NDG and M_1M_2-NDG, and E_{M_1/M_2}, U_{M_1/M_2} denote the formation energy and standard potential of the M_1/M_2 bulk phase[2], respectively.

Considering that the actual electrocatalytic reaction takes place in solution, and this electrochemical environment can be well described using the VASPsol method[3]. Furthermore, different applied potentials can be simulated by adding or removing electrons. The Debye screening length was set to 3.04 Å for setting the compensating background charge[4]. The relative dielectric constant is set to 78.4 for simulating an aqueous solution environment[5]. The electrochemical energy (E_{sol}) at different potentials can be expressed as:

$$E_{sol} = E_{VASP} - e\phi_{elyte}\Delta q - (\mu_e + e\phi_{elyte})\,\Delta q = E_{VASP} - E_F\Delta q \tag{17}$$

where E_{VASP} denotes the energy calculated by VASP and ϕ_{elyte} denotes the inherent electrostatic potential within the bulk electrolyte. μ_e and E_F denote the electrochemical potential and the Fermi level, respectively, whereas μ_e is equivalent to E_F in the Kohn-Sham-Mermin DFT method. Δq denotes the number of extra electrons[3]. For each intermediate, the extra electrons added to the system ranged from -2.0 e to +2.0 e in +0.4 e increments. Subsequently, we collected the free energy of the intermediates with different charge amounts for fitting, and calculated the reaction energy barrier curves of $*O_2$ activation ($\Delta G_{2\text{-SOL}}$) and *OH desorption ($\Delta G_{5\text{-SOL}}$) at different potentials according to the obtained free energy function of intermediates **(Fig. S47 to S52)**.

The electrode potential relative to the standard hydrogen electrode (U (V vs. SHE)) is defined as follows:

$$U\ (\text{V vs SHE}) = -4.44\text{V} - (E_F + E_{\text{fermishift}})/e \tag{18}$$

where $E_{\text{Fermishift}}$ is the corrected value of the Fermi level shift given by VASPsol, and 4.44V is the absolute electrode potential on the SHE scale[6, 7].

For the M_1M_2-NDG system the O_2 magnetic moment at the $*O_2$ is calculated as follows:

$$M = N(\text{spin-up}) - N(\text{spin-down}) \tag{19}$$

$$M = M(p_x) + M(p_y) + M(p_z) \tag{20}$$

where N(spin-up) and N(spin-down) represent the number of occupied state electrons in the spin-up *p* orbital and spin-down *p* orbital of O_2, respectively. $M(p_x)$, $M(p_y)$, and $M(p_z)$ represent the projections of O_2 magnetic moments on the p_x orbital, p_y orbital, and p_z orbital, respectively.

Besides, we employed the Bader code to quantify the amount of electron transfer upon adsorption of intermediate species by M_1M_2-NDG. In order to elucidate the contribution of local atomic orbital coupling to bonding, we have carried out the project crystal orbital Hamilton population (pCOHP) analysis[8] using LOBSTER software[9], and measured the bond strength of different orbital coupling by integrating the pCOHP below the Fermi level (ICOHP), where a more negative ICOHP indicates a more stable bonding between atoms.

Furthermore, in order to better observe the bonding mechanism of the intermediate states and the corresponding adsorption configurations, for the schematic diagrams of the adsorption modes, orbital Wannier function, and charge differential densities of the intermediates, we used the geometric model of M_1M_2-N6-C to replace the periodic

M_1M_2-NDG model in the diagram of the adsorption mode, charge differential density and orbital Wannier function for intermediates.

The thermodynamic stability tests of the six representative systems were achieved by Ab initio molecular dynamics (AIMD) simulations. A canonical ensemble (NVT) was used for the thermostat, setting the annealing temperature standard at 600 K and running for 8 ps with a 1fs time step.

Details of machine learning (ML) section:

The main idea of Crystal Graph Convolutional Neural Network (CGCNN)[10] is to obtain a crystal graph to represent the crystal structure by encoding the atomic information and bonding interactions between atoms, and then train it by convolutional neural network with the collected DFT computational data and predict the target properties (Overpotential and PDS). In CGCNN, each atom node i is represented by a feature vector v_i and the corresponding encoding represents the atomic properties. Similarly for the k-th edge $(i,j)_k$ formed between the atom node i and the nearest neighbor atom node j is represented by the feature vector $u_{(i,\ j)k}$. The overall convolutional neural network can be divided into two parts: the convolutional layer and the pooling layer. The specific workflow of CGCNN is as follows:

Firstly, the convolution layer is convolved with the surrounding atoms as well as the corresponding chemical bonds through a nonlinear map convolution function, and the atom feature vector v_i is iterated over and over again, and the corresponding equations are as follows:

$$\boldsymbol{z}_{(i,j)_k}^{(t)} = \boldsymbol{v}_i^{(t)} \oplus \boldsymbol{v}_j^{(t)} \oplus \boldsymbol{u}_{(i,j)_k} \tag{21}$$

$$\boldsymbol{v}_i^{(t+1)} = \boldsymbol{v}_i^{(t)} + \sum_{j,k} \sigma\left(\boldsymbol{z}_{(i,j)_k}^{(t)} \boldsymbol{W}_f^{(t)} + \boldsymbol{b}_f^{(t)}\right) \odot g\left(\boldsymbol{z}_{(i,j)_k}^{(t)} \boldsymbol{W}_s^{(t)} + \boldsymbol{b}_s^{(t)}\right) \tag{22}$$

Where $\boldsymbol{z}_{(i,j)_k}^{(t)}$ denotes first concatenates neighbor vector of the t-th layer, $\oplus$ denotes concatenation of atom and bond feature vectors; $\odot$ denotes the dot product of the matrix; σ and g denote the nonlinear activation functions, $\boldsymbol{W}_f^{(t)}$ and $\boldsymbol{W}_s^{(t)}$ denote the convolutional weight matrix and the self-weight matrix of the t-th layer, and $\boldsymbol{b}_f^{(t)}$ and $\boldsymbol{b}_s^{(t)}$ denote the bias in the neural network of the t-th layer. Subsequently, the pooling layer averages the feature vectors v_i of all convolutional layer to obtain the global property v_c:

$$\boldsymbol{vc} = \frac{1}{\mathrm{N}} \sum_{\mathrm{i}} \boldsymbol{v}_i^{(t)} \tag{23}$$

where N denotes the number of atoms in the input crystal material.

Eventually, after the training of the global property v_c is completed, the model learns the contribution of the local chemical environment represented by each v_i through multiple hidden layers, and finally outputs the predicted target property through the fully-connected layer ($\Delta G_{\mathrm{ORR,\ ML}}$ for the regression model and $\mathrm{PDS}_{\mathrm{ORR,\ ML}}$ for the classification model).

Subsequently, in the comparison of the prediction results of different models, we firstly took Graph Networks (MEGnet)[11], which is also a neural network widely used in crystallography, the principle of this network is similar to CGCNN, but the parameters related to the global state are introduced to aggregate all the environment vectors using the global attention layer.

The remaining Random Forest (RF), Support Vector Machine (SVM), and Gradient Boosting Decision Tree (GBDT) are traditional ML methods that can be invoked via the scikit-learn library in python[12]. For the inputs to these models, we used the Orbital Field Matrix (OFM)[13] methods to construct the associated feature vectors.

Figure S1~S52 and Note S1~12:

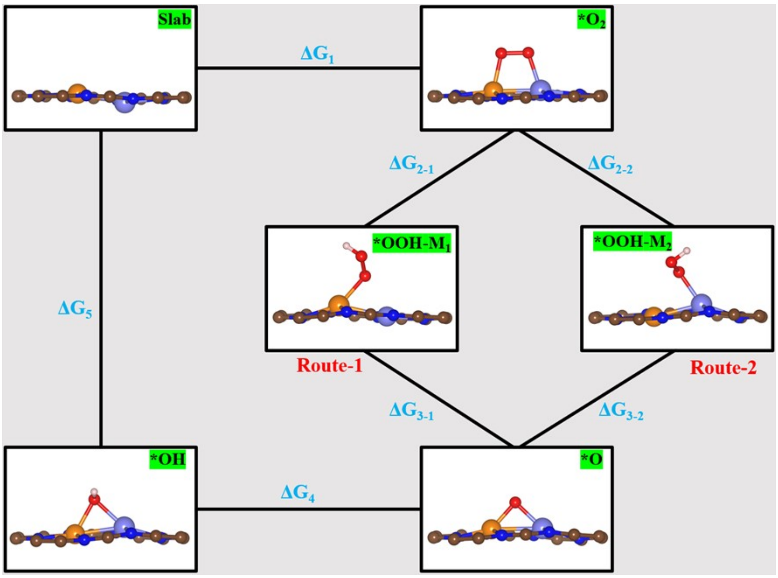

Figure S1 Different reaction paths of heteronuclear M_1M_2-NDG.

Note S1 Selection of different reaction paths for heteronuclear M_1M_2-NDG:

For the homonuclear M_1M_2-NDG, there are no different reaction paths since the M_1, M_2 atom is equivalent and the overall structure has symmetry. However, for heteronuclear M_1M_2-NDG, M_1 and M_2 atom are not equivalent, so some intermediate species may adsorb to different metal sites to form different intermediates. For example, OOH adsorbed to different metal sites will form different intermediates ($*OOH-M_1$,

$*OOH-M_2$ in **Fig. S1**). In this case, we will choose the route (Route-1, Route-2) with lower total energy as the reaction path. The specific rules are as follows:

$$\Delta G_{Route\text{-}1} = \max(\Delta G_{2\text{-}1}, \Delta G_{3\text{-}1}) \tag{24}$$

$$\Delta G_{Route\text{-}2} = \max(\Delta G_{2\text{-}2}, \Delta G_{3\text{-}2}) \tag{25}$$

$$\Delta G_{Route}, i = \min(\Delta G_{Route\text{-}1}, \Delta G_{Route\text{-}2}), \mathrm{Best}(\text{Route-1}, \text{Route-2}) \tag{26}$$

$$\Delta G_2 = \Delta G_{2\text{-}i}, \Delta G_3 = \Delta G_{3\text{-}i} \tag{27}$$

where $\Delta G_{route\text{-}1}$, $\Delta G_{route\text{-}2}$ denote the highest reaction energy barrier in Route 1 and Route 2 from $*O_2$ to O, respectively, while i, ΔG_{Route} denote the route with lower highest reaction energy barrier in Route 1 and Route 2 as well as the corresponding reaction energy barriers, respectively, so the value of i is in 1, 2. Finally, we chose this route as the ORR path for this system in the DFT calculations.

Note S2 Four coordination modes extracted from M_1M_2-NDG:

When M_1M_2 is used as a coordination mode (Including M_1 atom, M_2 atom), only the M_1, M_2 atom and the bonding between them are considered as the feature vectors input to the model. When M_1M_2-N6 is used as a coordination mode (Including M_1 atom, M_2 atom, 6 N atoms), on top of M_1M_2, the feature vectors must also take into account the 6 nearest neighboring N atoms as well as the formation of the M1/M2-N bonds. When M_1M_2-N6-C is used as a coordination mode (Including M_1 atom, M_2 atom, 6 N atoms, 10 C atoms), on top of M_1M_2-N6, the feature vectors also take into account the enclosing C atoms as well as the formed C-N bond and C-C bond. When M_1M_2-NDG is used as a coordination mode (Including M_1 atom, M_2 atom, 6 N atoms, 40 C atoms), the feature vector will include all atoms in the supercell and the corresponding bonding.

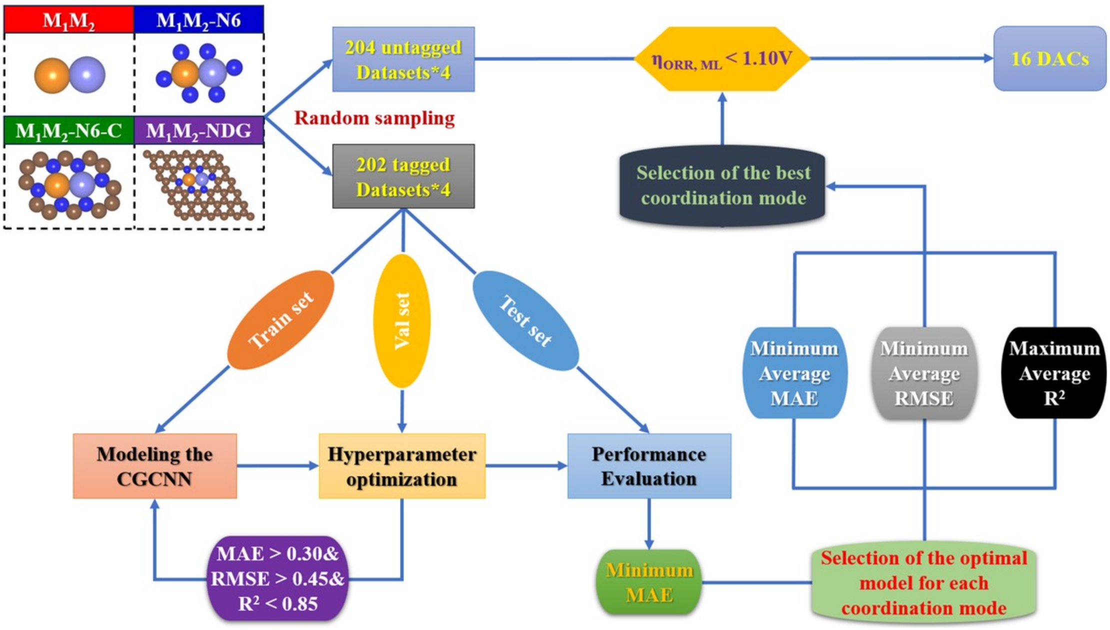

Figure S2 Workflow of the CGCNN regression model.

Note S3 Workflow of the CGCNN regression model construction and screening:

In constructing the CGCNN regression model, the 202 tagged datasets under each coordination mode are randomly divided into train set (containing 162 DACs), validation set (contain 20 DACs), and test set (containing 20 DACs) in the ratio of 8:1:1. Firstly, the initial CGCNN regression model with hyperparameters (see **Table S1~S4** for details of the relevant hyperparameters) is constructed through the train set, and then its generalization ability is evaluated by observing the performance of the model on the validation set. The evaluation criteria flow is as follows, if the output result of the model on the validation set has any of MAE > 0.3, RMSE > 0.45, $R^2 < 0.85$, we will consider the model has poor generalization ability and discard the model, and re-select the hyperparameters to start the next round of CGCNN regression model construction. Otherwise, this CGCNN regression model is exported to the test set for testing, while keeping the test results with hyperparameters and fine-tuning the hyperparameters to construct the next round of CGCNN regression model. The entire process described above is referred to as a trial, and for each coordination mode, we conducted at least 200 such trials to ensure at least 20 CGCNN regression models with different hyperparameters that passed the screening. Finally, among the many CGCNN regression models that passed the screening, the CGCNN regression model that exhibited the smallest MAE value on the test set was considered the optimal CGCNN regression model for that coordination mode.

At this point, we extract the optimal CGCNN regression model from each of the four coordination modes and compare them to choose the most appropriate coordination mode (MAE, RMSE, R^2 are still used as evaluation metrics). Furthermore, in order to reduce the error of the test results due to sampling chance (well or poorly fitted dataset due to improper sampling), we used random seeds to divide the tagged dataset several times, and created train set, validation set, and test set with different combinations of samples. Subsequently, we counted the test results (MAE, RMSE, R^2) of the CGCNN regression model with each coordination modes for the train set, validation set, and test set under each random seed, and plotted them as box plots (**Fig. S3**) in order to make a comprehensive assessment of their prediction performance and generalization ability.

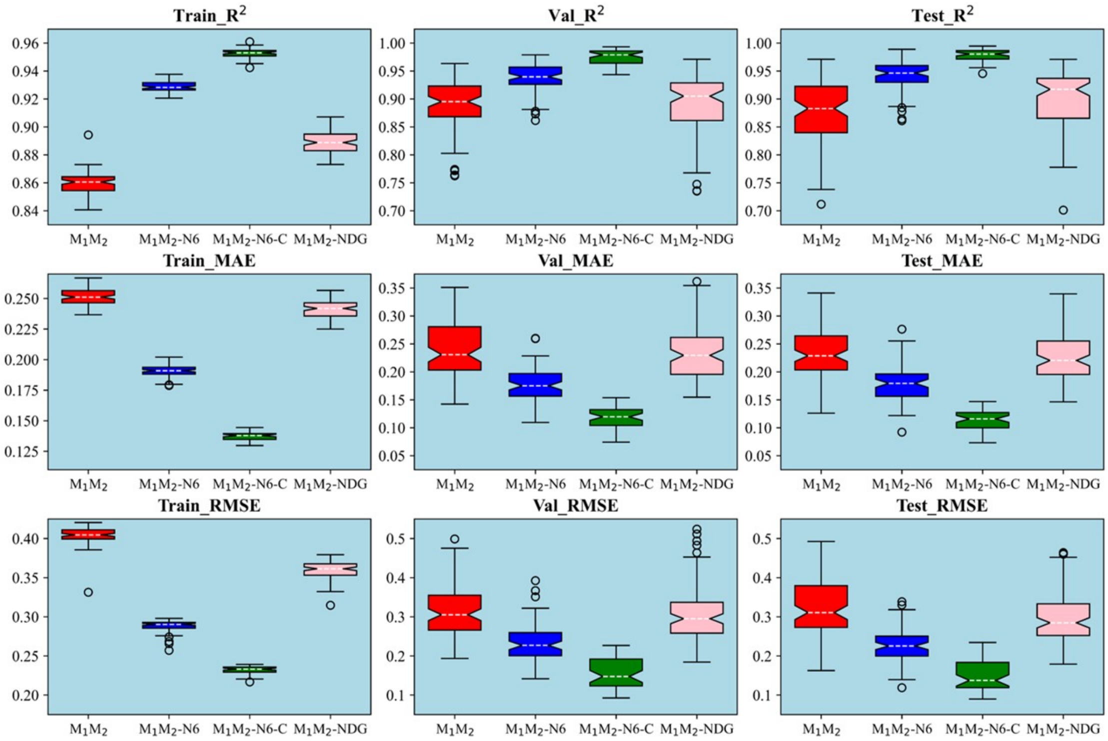

Figure S3 The evaluation results (R^2, MAE, RMSE) box plots of the CGCNN regression model with different coordination modes on multiple train, validation and test sets.

As shown in **Fig. S3**, the box plots provide a good representation of the comprehensive performance of all the random seeds on our train, validation, and test sets. For the CGCNN regression model with M_1M_2, it can be seen that the model performance is a bit unsatisfactory. Although the $R^2 > 0.85$ and MAE < 0.25 for most of the datasets, the RMSE on a considerable portion of the data is greater than 0.3 on both the train sets and test sets, and even reaches more than 0.4 on the train sets, which suggests that the model gives a large deviation between the predicted value and the actual value of some of the samples, and is in the state of underfitting. After incorporating C, N atoms into the coordination environment, the quality of the CGCNN regression model is significantly improved (R^2 increases, MAE, RMSE decreases on the train set), and the generalization error also decreases (R^2 increases, MAE, RMSE decreases on the validation set, test set). Among them, the CGCNN regression model with M_1M_2-N6-C achieves the best prediction performance on the total dataset, with MAE less than 0.15 V on the majority of datasets, and the average MAE on multiple test sets was only 0.13 V. However, if the entire NDG is taken into account as a coordinated environment, the fitting and generalization ability of the model decreases instead (With a decrease in R^2, an increase in MAE, and an increase in RMSE relative to M_1M_2-N6, M_1M_2-N6-C). Eventually, we obtained the most appropriate coordination mode (M_1M_2-N6-C) and the corresponding optimal CGCNN regression model.

Note S4 Screening process for promising DACs on untagged dataset

We called the optimal CGCNN regression model in the M_1M_2-N6-C coordination mode to predict the $\eta_{ORR,\ ML}$ of the tagged dataset to filter out the DACs below the overpotential threshold in the untagged dataset, where the overpotential threshold is defined as follows: the ORR overpotential of the Pt/C catalyst to be 0.97 V (**Table S5**), while the average MAE obtained on multiple test sets using the optimal CGCNN regression model in the M_1M_2-N6-C coordination mode was 0.13 V. Therefore, 1.10 V (0.97 + 0.13) was adopted as the overpotential threshold for screening the promising DACs in the untagged dataset. Ultimately, we harvested 16 promising DACs from the untagged dataset, and calculated their corresponding $\eta_{ORR,\ DFT}$.

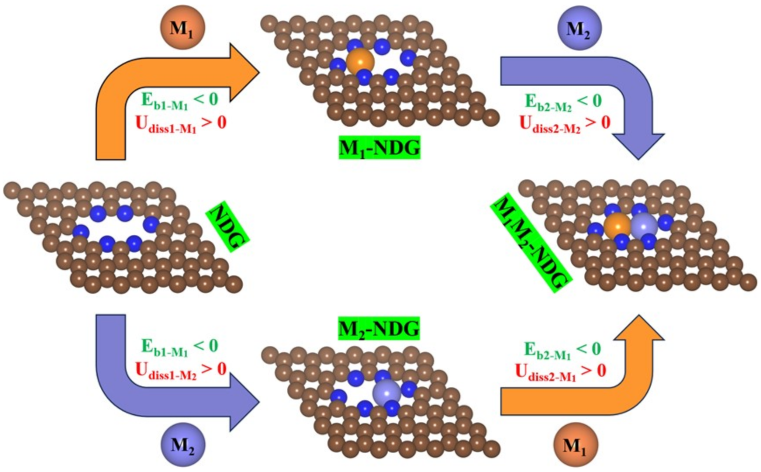

Figure S4 Stability evaluation process of M_1M_2-NDG.

Note S5 The definition of stability metric, selectivity metric and ORR activity metric

Stability metric: In general, the negative formation energy (E_f) indicates the M_1, M_2 atom can theoretically be embedded in the central vacancy of the NDG, whereas a positive dissociation energy (U_{diss}) indicates that the M_1, M_2 atom are difficult to dissociate from the NDG. As shown in **Fig. S4**, our process for evaluating the stability of M_1M_2-NDG catalyst is as follows: firstly at least one of its M_1 atom or M_2 atom can be anchored in the central vacancy of the NDG to form an M_1/M_2-NDG ($E_{b1\text{-}M_1}/E_{b2\text{-}M_2} < 0$), and make sure that they do not desorb from the NDG to aggregate into the bulk phase ($U_{diss1\text{-}M_1}/U_{diss1\text{-}M_2} > 0$). Subsequently, the M_1/M_2-NDG combines with M_2/M_1 atom to obtain M_1M_2-NDG, which again needs to pass a similar judgment condition as before ($E_{b2\text{-}M_2}/E_{b2\text{-}M_1} < 0$ and $U_{diss2\text{-}M_2}/U_{diss2\text{-}M_1} > 0$). The M_1M_2-NDG that ultimately satisfies both of these conditions is the stabilized system we are aiming for.

Selectivity metric: To ensure that a four-electron ORR occurs rather than a two-electron ORR (The reduction product is H_2O and not H_2O_2), *O should be formed more easily than H_2O_2 during the ORR, i.e. $G_{*O} + G_{H2O} < G_{Slab} + G_{H2O2}$, Where G_{H2O2} represents the free energy of H_2O_2.

ORR activity metric: The theoretical overpotential calculated by DFT of M_1M_2-NDG is lower than the Pt/C, i.e., $\eta_{ORR,\ DFT} < 0.97$ V.

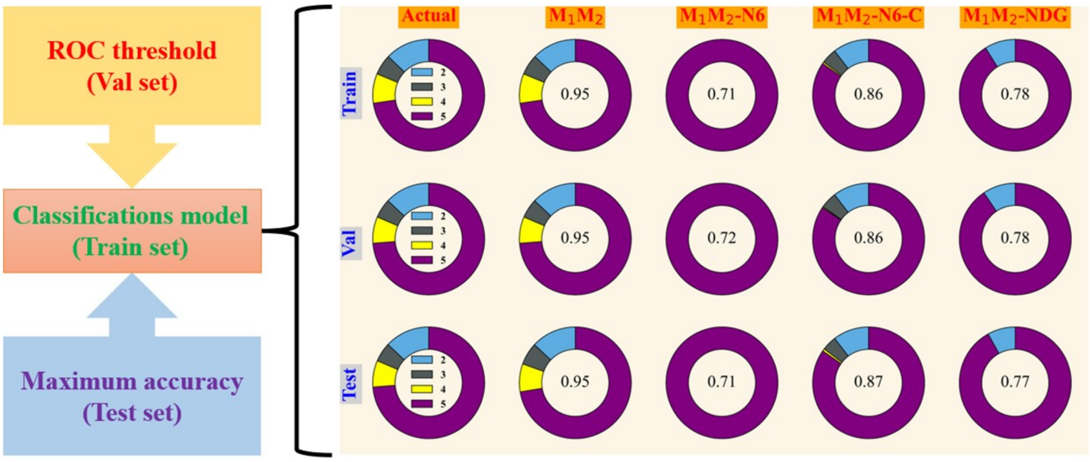

Figure S5 The evaluation results (Accuracy) donuts of the CGCNN classification model with different coordination modes on multiple train, validation and test sets (Where the different colors in the circles represent the percentage of different reaction steps, in which the first step of O_2 adsorption is spontaneous in all systems, and therefore only step2~step5 were considered. The number in the circle center indicates the average accuracy).

Note S6 Screening process for CGCNN classification models:

Similar to the process of screening regression models, the train set is used to initially construct the classification model, the validation set retains the classification models that above the ROC threshold, and the test set filters out the optimal CGCNN classification model with maximum accuracy. Finally, the average of the prediction accuracy of multiple random seeds under the four coordination modes was compared.

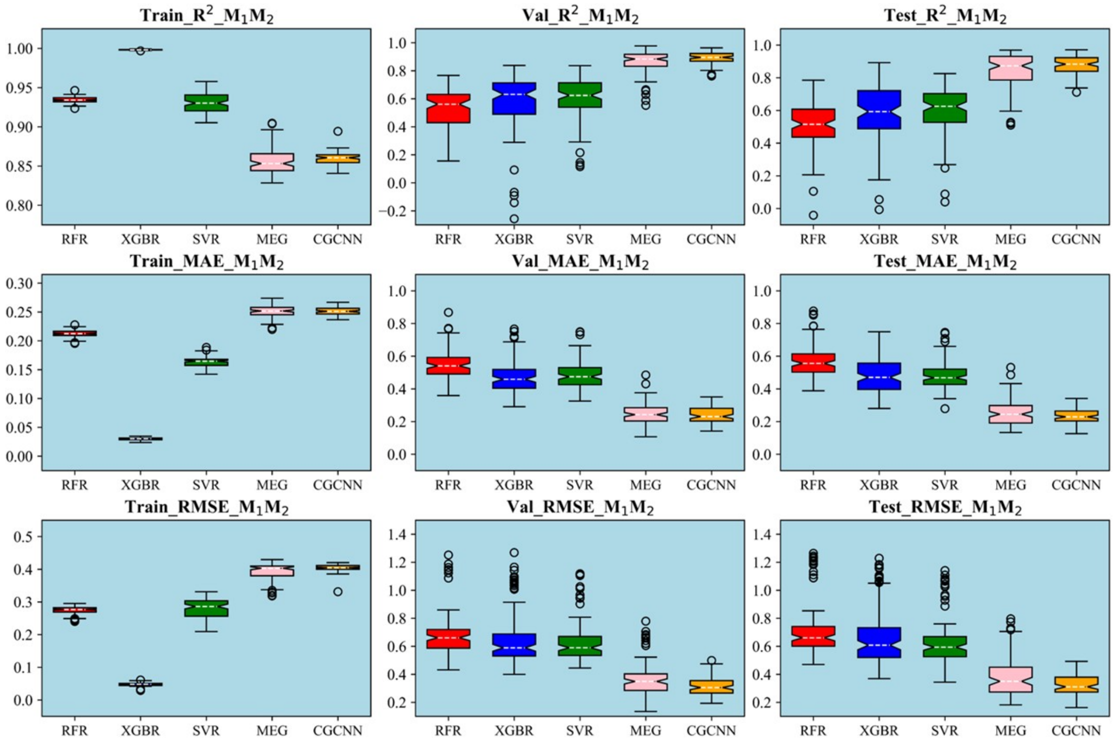

Figure S6 The evaluation results (R^2, MAE, RMSE) box plots of different regression models with M_1M_2 on multiple train, validation, and test sets.

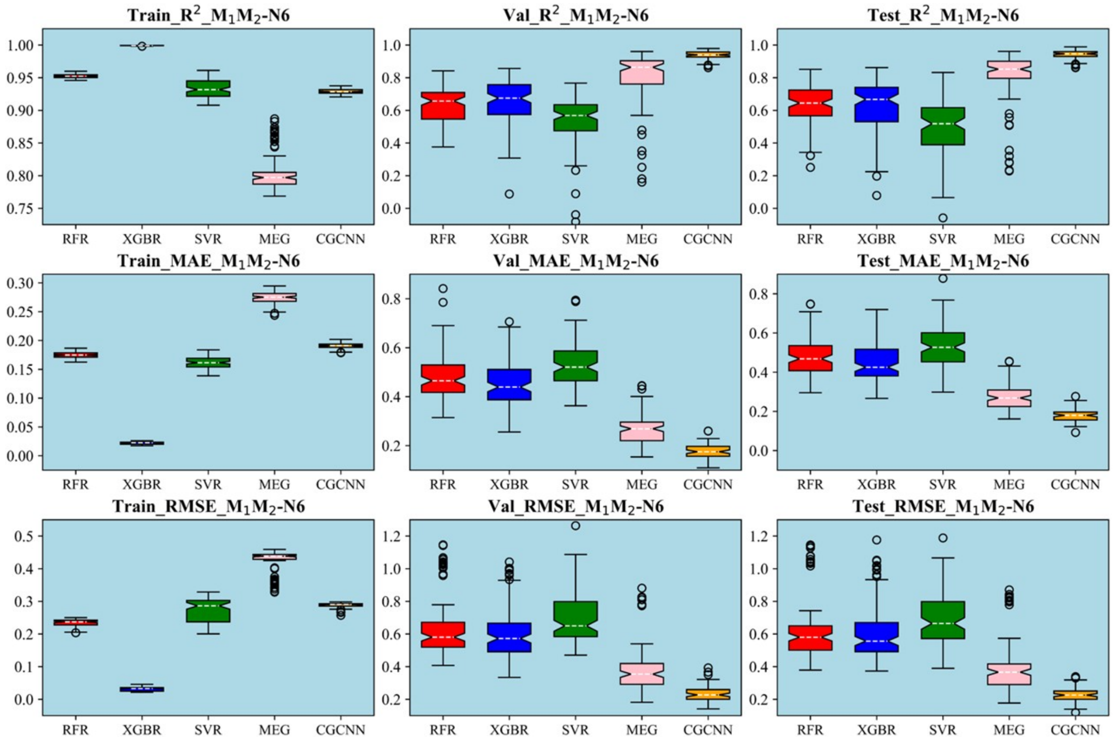

Figure S7 The evaluation results (R^2, MAE, RMSE) box plots of different regression models with M_1M_2-N6 on multiple train, validation, and test sets.

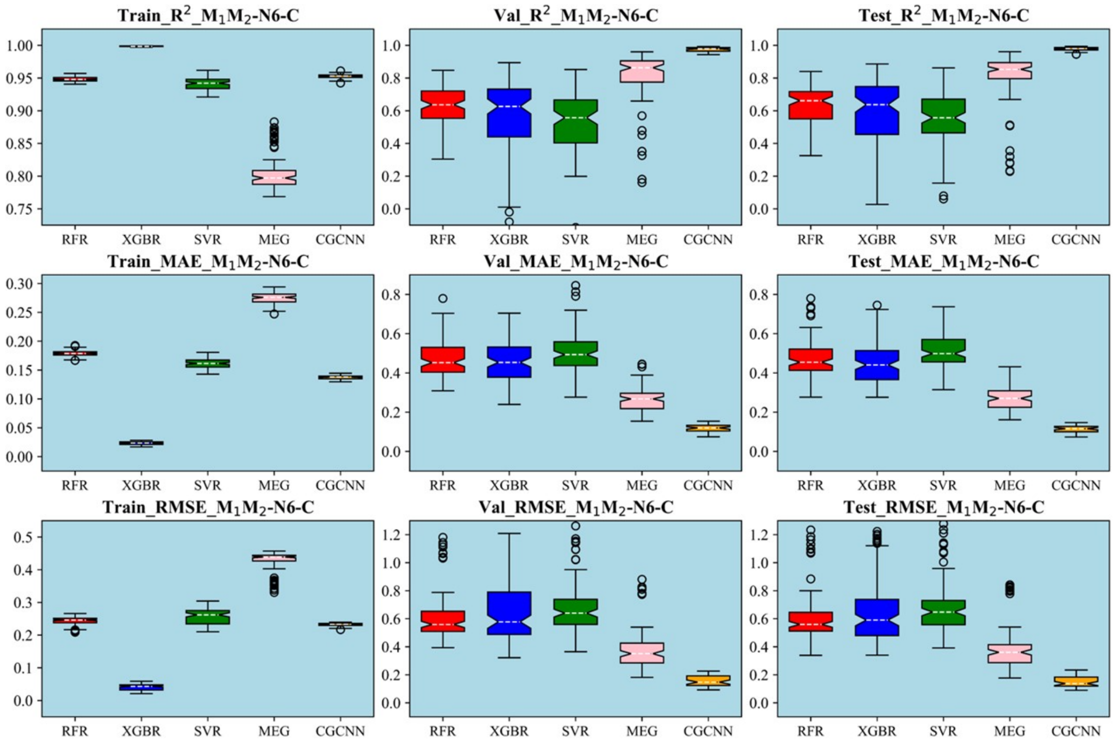

Figure S8 The evaluation results (R^2, MAE, RMSE) box plots of different regression models with M_1M_2-N6-C on multiple train, validation, and test sets.

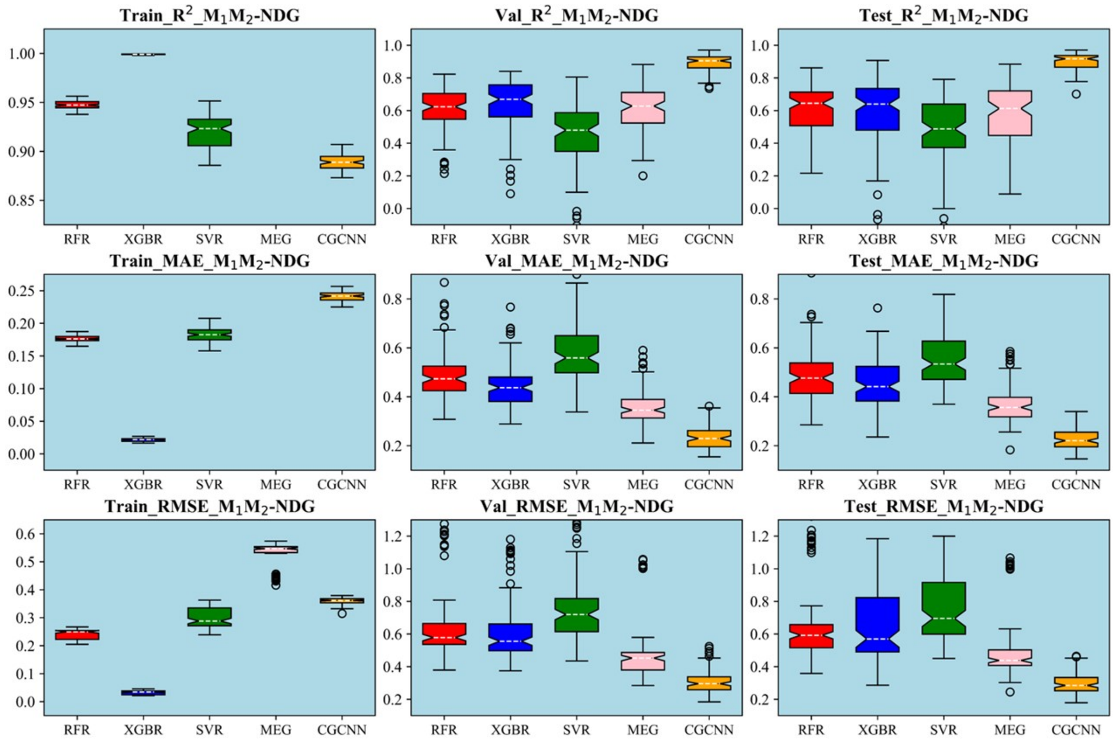

Figure S9 The evaluation results (R^2, MAE, RMSE) box plots of different regression models with M_1M_2-NDG on multiple train, validation, and test sets.

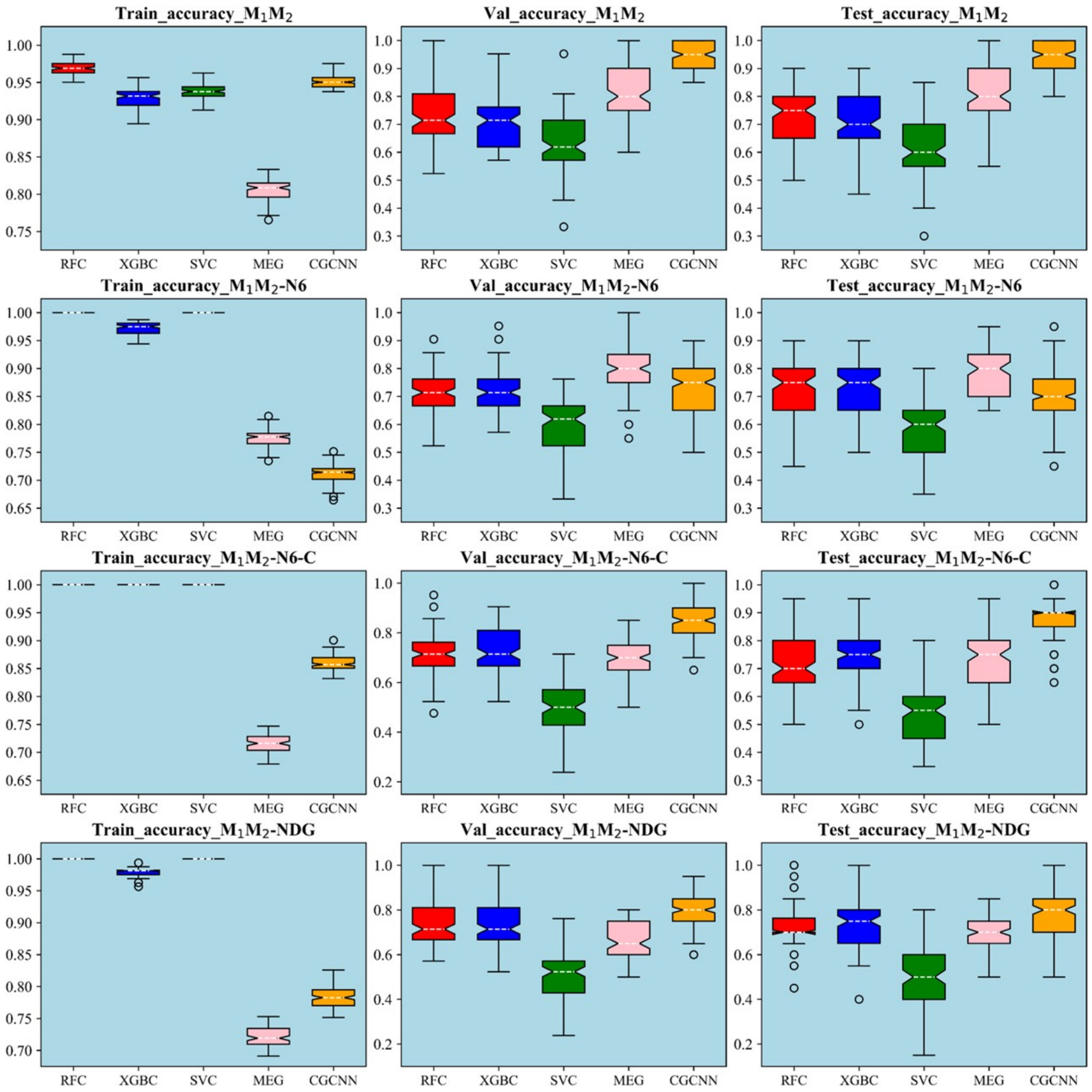

Figure S10 The evaluation results (Accuracy) box plots of different classification models on multiple train, validation, and test sets under four coordination modes.

Note S7 CGCNN model compared to other ML models:

Firstly, for the regression model (**Fig. S6 ~ Fig. S9**), although RFR, XGBR, SVR outperform MEG and CGCNN on the train set, their prediction errors on the validation and test sets are significantly higher, which indicates that these three traditional ML models are in an overfitting state and have poor generalization ability. As for MEG, its prediction performance of mode is inferior to that of CGCNN in all four coordination modes. As for the classification model (**Fig. S10**), similar to the findings for the regression model, the traditional ML models still suffer from overfitting. Although the accuracy of MEG (Accuracy around 0.8) with M_1M_2-N6 is higher than that of CGCNN, it still does not exceed that of CGCNN with M_1M_2 (Accuracy close to 0.95). In summary, in this paper, CGCNN achieves better fitting results when dealing with both regression and classification problems compared to other ML models.

Note S8 Limitations and Outlook of the CGCNN model:

In our study, the coordination environments were fixed, which could lead to the CGCNN model defaulting to a learning process in which the coordination environments of different samples did not play a significant difference in the modulation of catalytic activity. For example, the input of the feature vector of coordination environment is 0 for all samples, which naturally has a minimal effect on the prediction results. However, in fact, many studies[14,16] have shown that atom doping, substrate defects in the coordination environment are of significant influence, which results the prediction results of our model may have a large deviation when facing this kind of DACs system. Therefore, by introducing other types of coordination environments (e.g., pure graphene substrate, varying the coordination number of nearest neighbor N atoms) to increase the combination of substrate and dual-atom, the CGCNN model can better perceive the role played by the coordination environment in modulating the catalytic activity, which in turn improves the ability of model to generalize in the face of a variety of DACs.

Moreover, the model currently does not consider the reaction mechanism adopted during catalysis to be converted into feature vector (e.g. setting the dissociation mechanism as 0 and the association mechanism as 1 in the feature vector), but often the actual reaction mechanism adopted by the catalyst actually determines its overpotential and PDS to a large extent. Therefore, if the reaction mechanism is extracted as a feature vector input, it can theoretically further facilitate the learning of the kernel essence of the catalytic reaction by the CGCNN model.

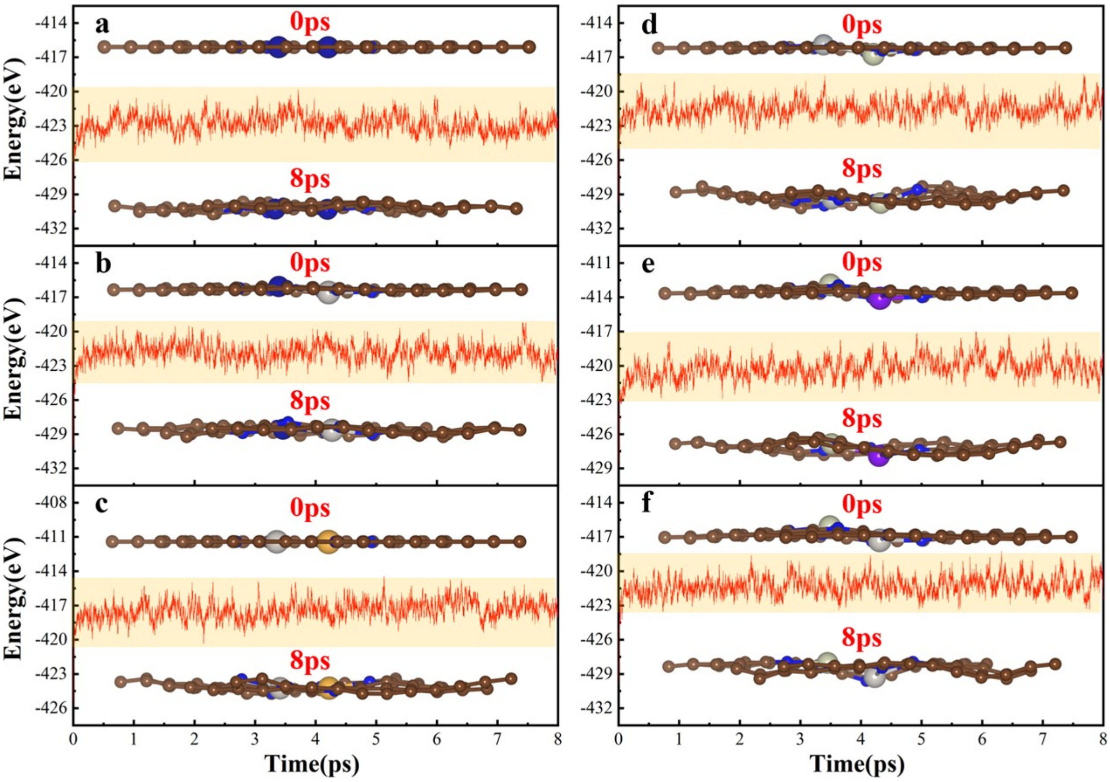

Figure S11 AIMD simulation of a. CoCo-NDG, b. CoPt-NDG, c. PtAu-NDG, d. NiRh-NDG, e. RhPd-NDG, and f. RhPt-NDG.

Note S9 Thermodynamic stability verification of 6 representative systems:

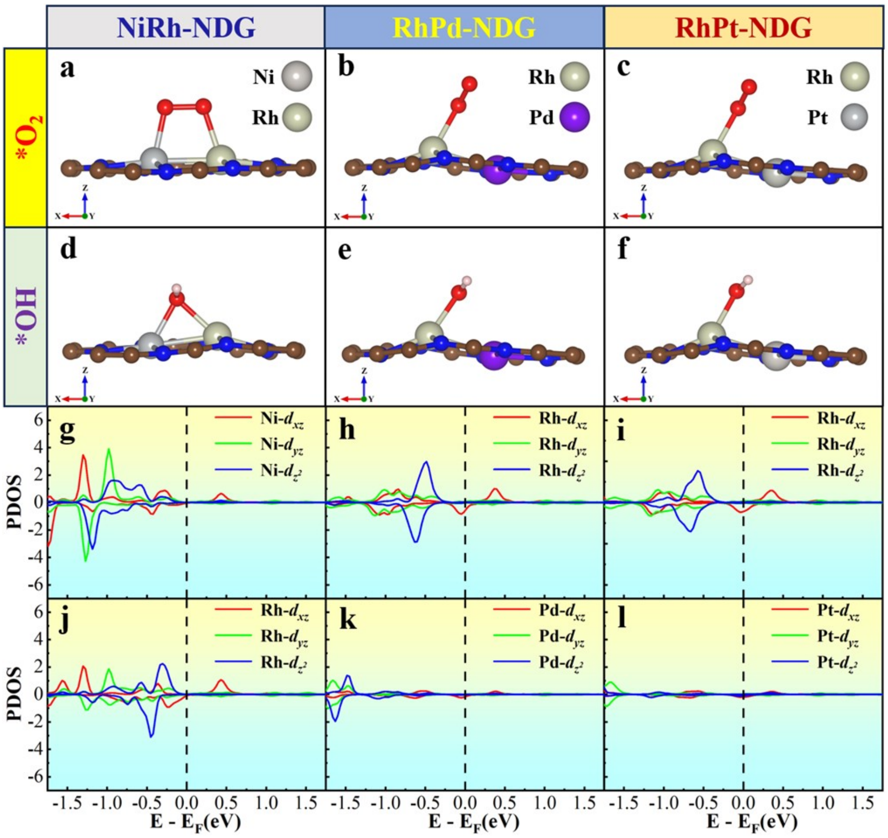

Figure S12 Front view of a. NiRh-NDG&O_2, b. RhPd-NDG&O_2, and c. RhPt-NDG&O_2; d. NiRh-NDG&OH, e. RhPd-NDG&OH, and f. RhPt-NDG&OH; the d_{xz}, d_{yz}, d_{z^2} orbital DOS near Fermi level of M_1 atom in g. NiRh-NDG, h. RhPd-NDG, and i. RhPd-NDG; the d_{xz}, d_{yz}, d_{z^2} orbital DOS near the Fermi level of M_2 atom in j. CoCo-NDG, k. CoPt-NDG, and l. PtAu-NDG.

As shown in **Fig. S11**, although the energy of M1M2-NDG fluctuates with time at high temperature (600K), the overall energy varies up and down by a small amount (light orange region), hovering only between a few eV. Subsequently, we further observed the changes of geometric morphology before and after the annealing (0 ps and 8 ps), and one can be seen that the originally flat NDG substrate is slightly distorted after annealing, but the M_1, M_2 atom in the center of NDG were always firmly anchored between the 6 N atoms (Not detached from the substrate), which implies that the six representative systems still have a good thermodynamic stability even at high temperature.

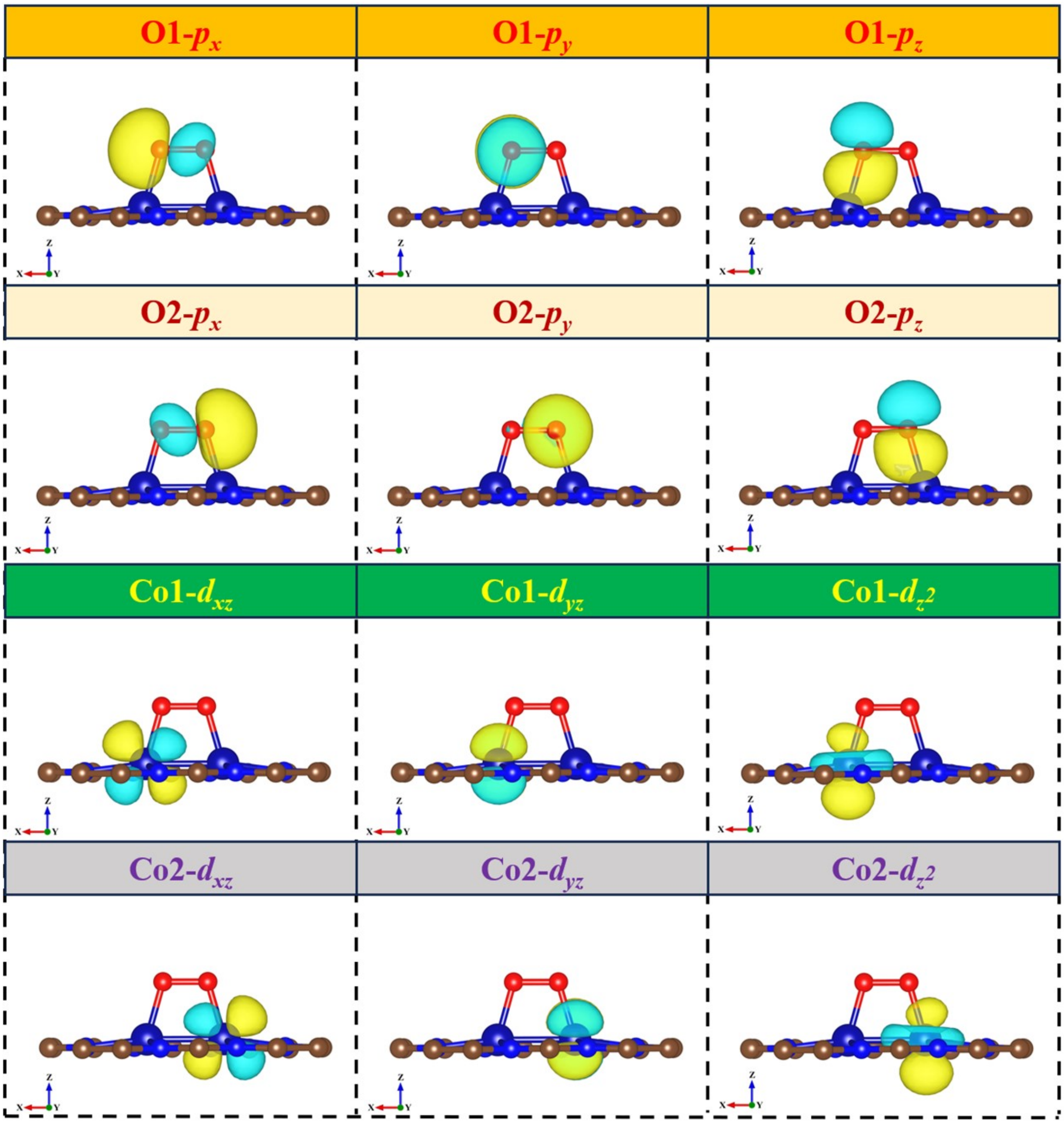

Figure S13 The d_{xz}, d_{yz}, d_{z^2} orbital Wannier function of Co1, Co2 atom and the p_x, p_y, p_z orbital Wannier function of O1, O2 atom in CoCo-NDG&O_2.

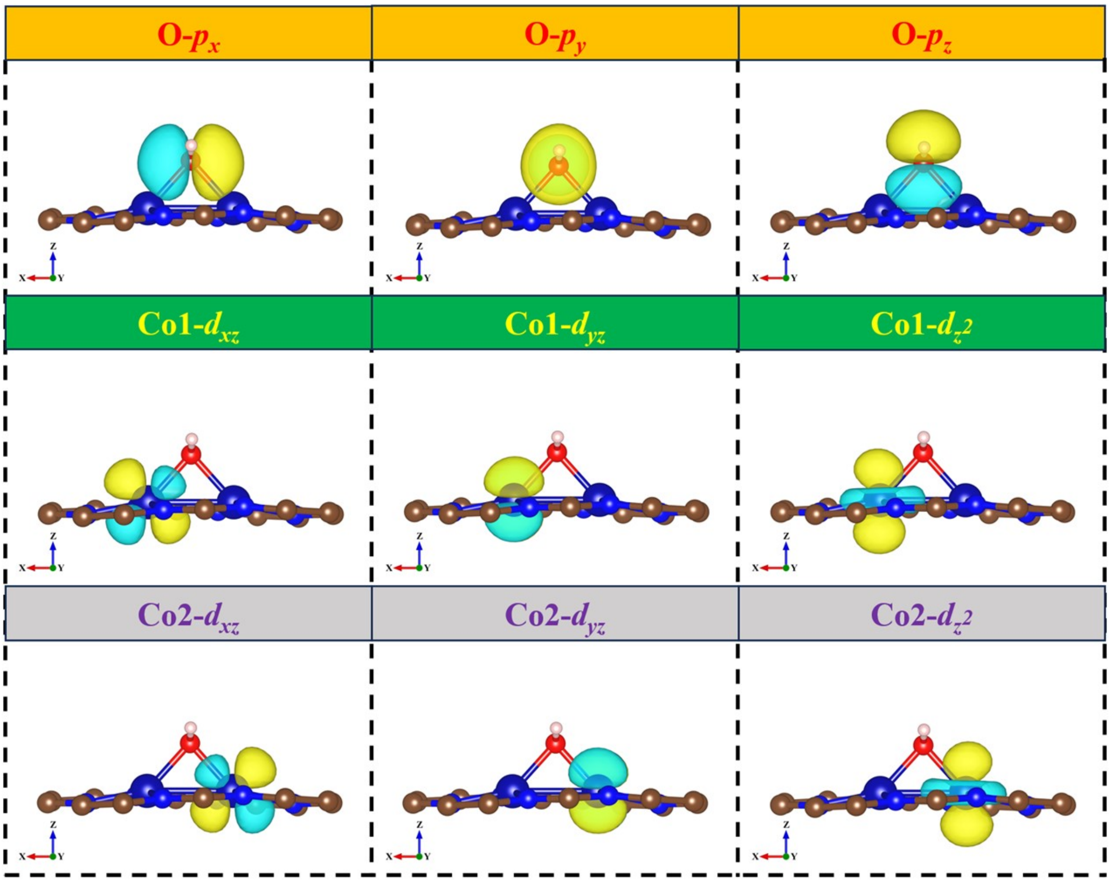

Figure S14 The d_{xz}, d_{yz}, d_{z^2} orbital Wannier function of Co1, Co2 atom and the p_x, p_y, p_z orbital Wannier function of O atom in CoCo-NDG&OH.

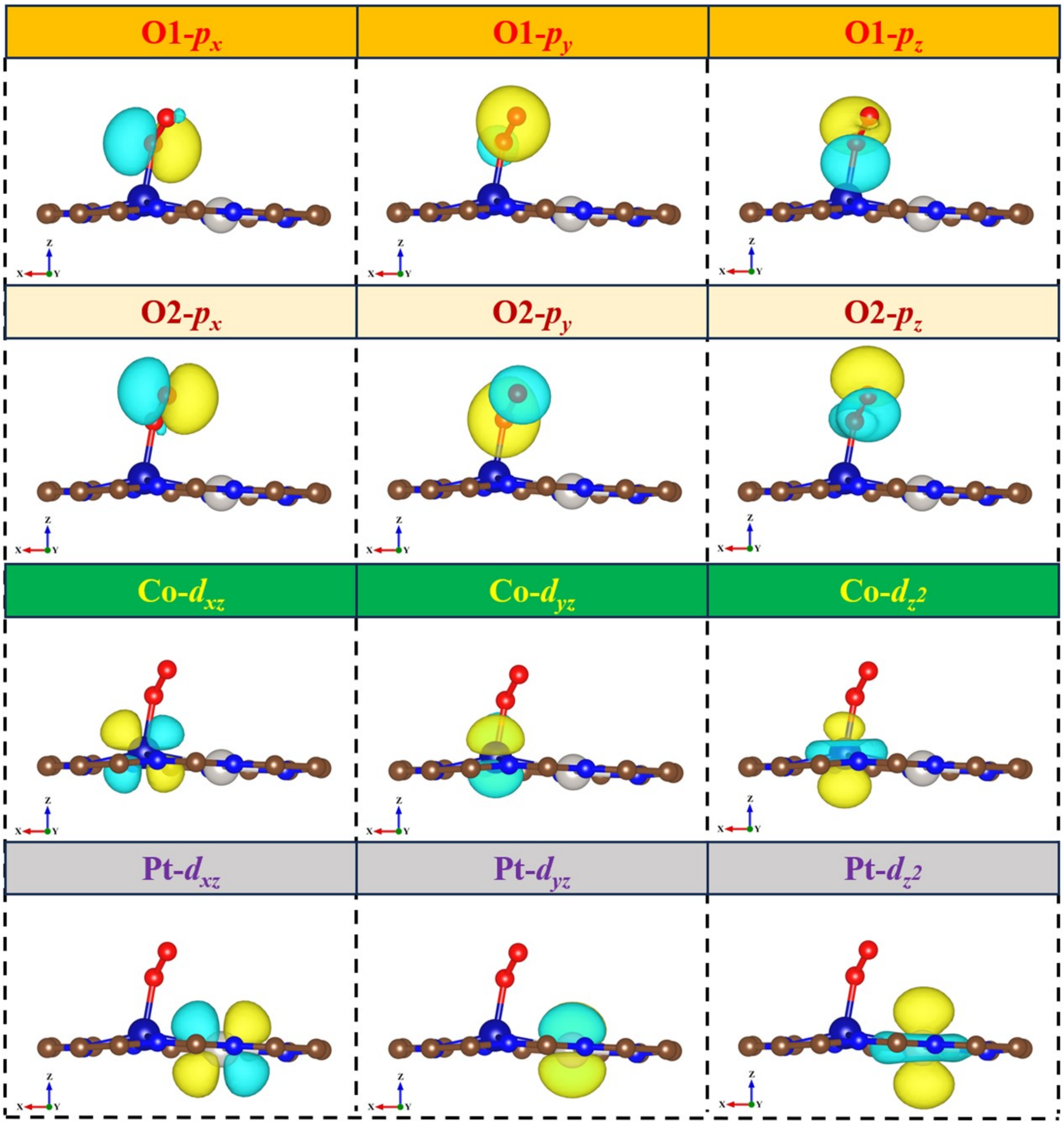

Figure S15 The d_{xz}, d_{yz}, d_{z^2} orbital Wannier function of Co, Pt atom and the p_x, p_y, p_z orbital Wannier function of O1, O2 atom in CoPt-NDG&O_2.

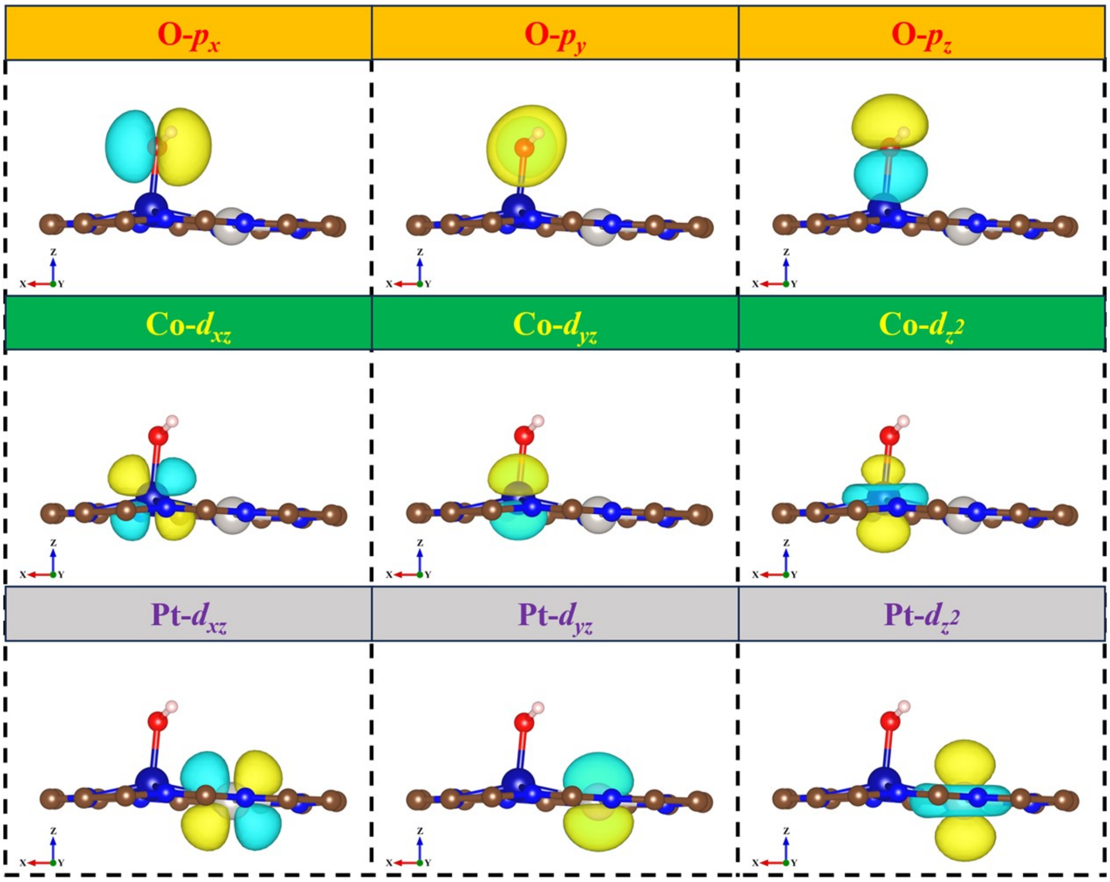

Figure S16 The d_{xz}, d_{yz}, d_{z^2} orbital Wannier function of Co, Pt atom and the p_x, p_y, p_z orbital Wannier function of O atom in CoPt-NDG&OH.

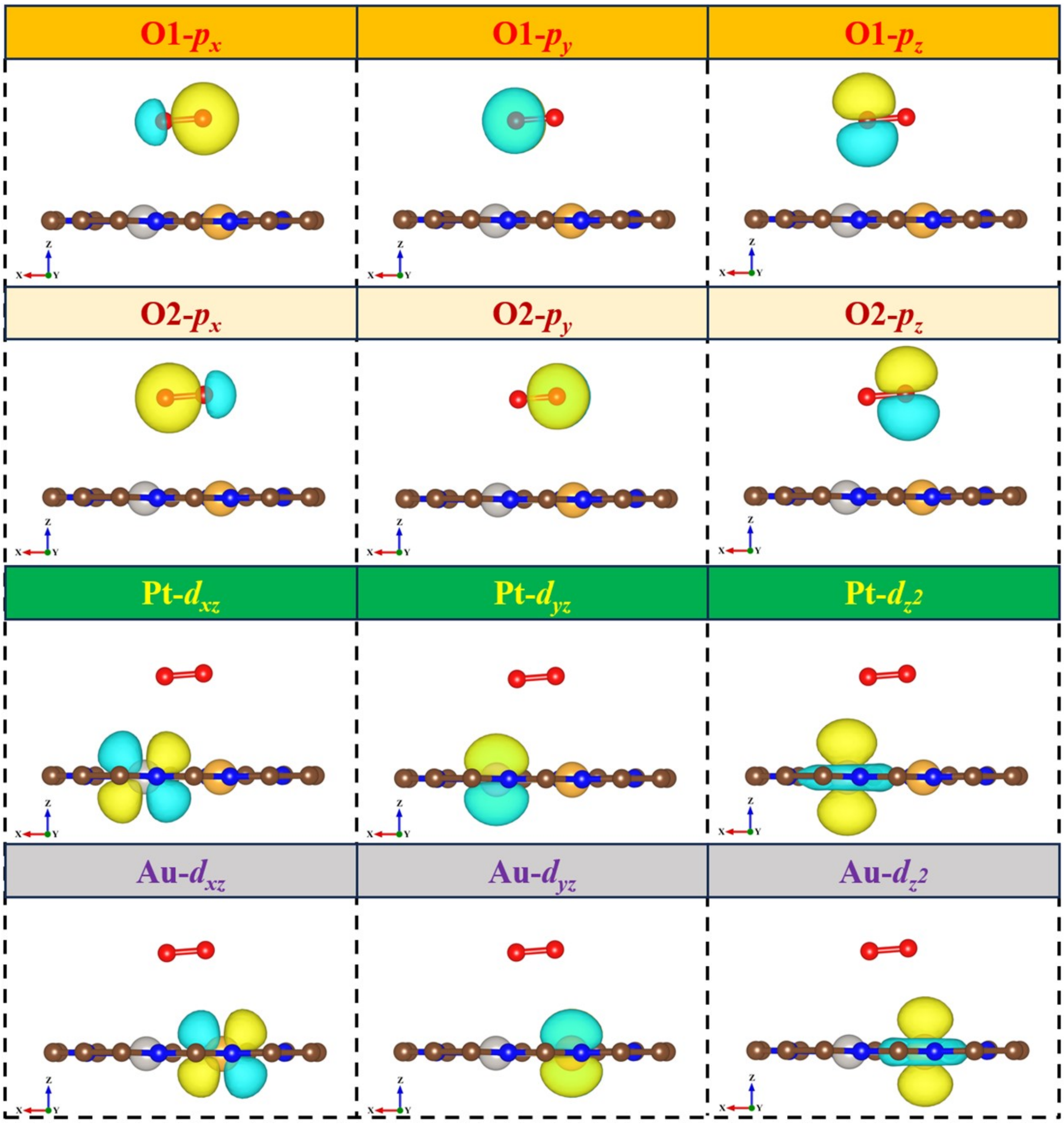

Figure S17 The d_{xz}, d_{yz}, d_{z^2} orbital Wannier function of Pt, Au atom and the p_x, p_y, p_z orbital Wannier function of O1, O2 atom in PtAu-NDG&O_2.

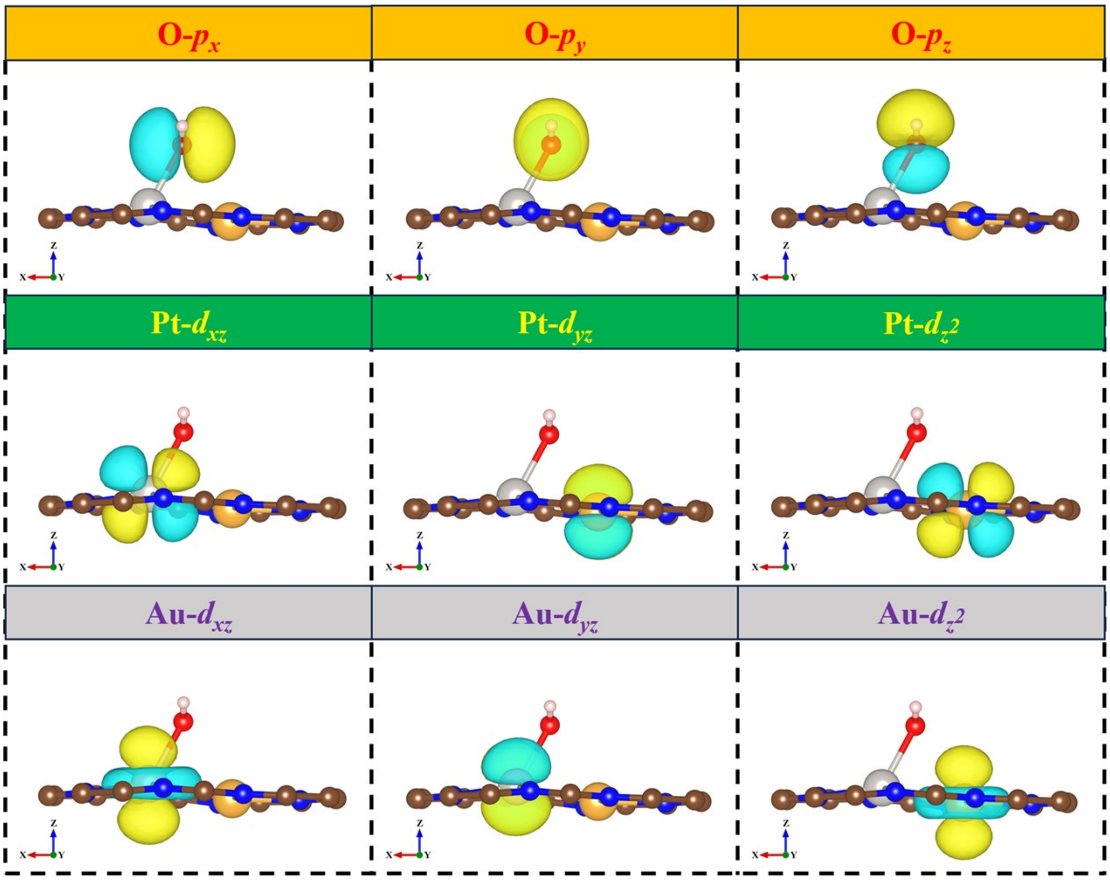

Figure S18 The d_{xz}, d_{yz}, d_{z^2} orbital Wannier function of Pt, Au atom and the p_x, p_y, p_z orbital Wannier function of O atom in PtAu-NDG&OH.

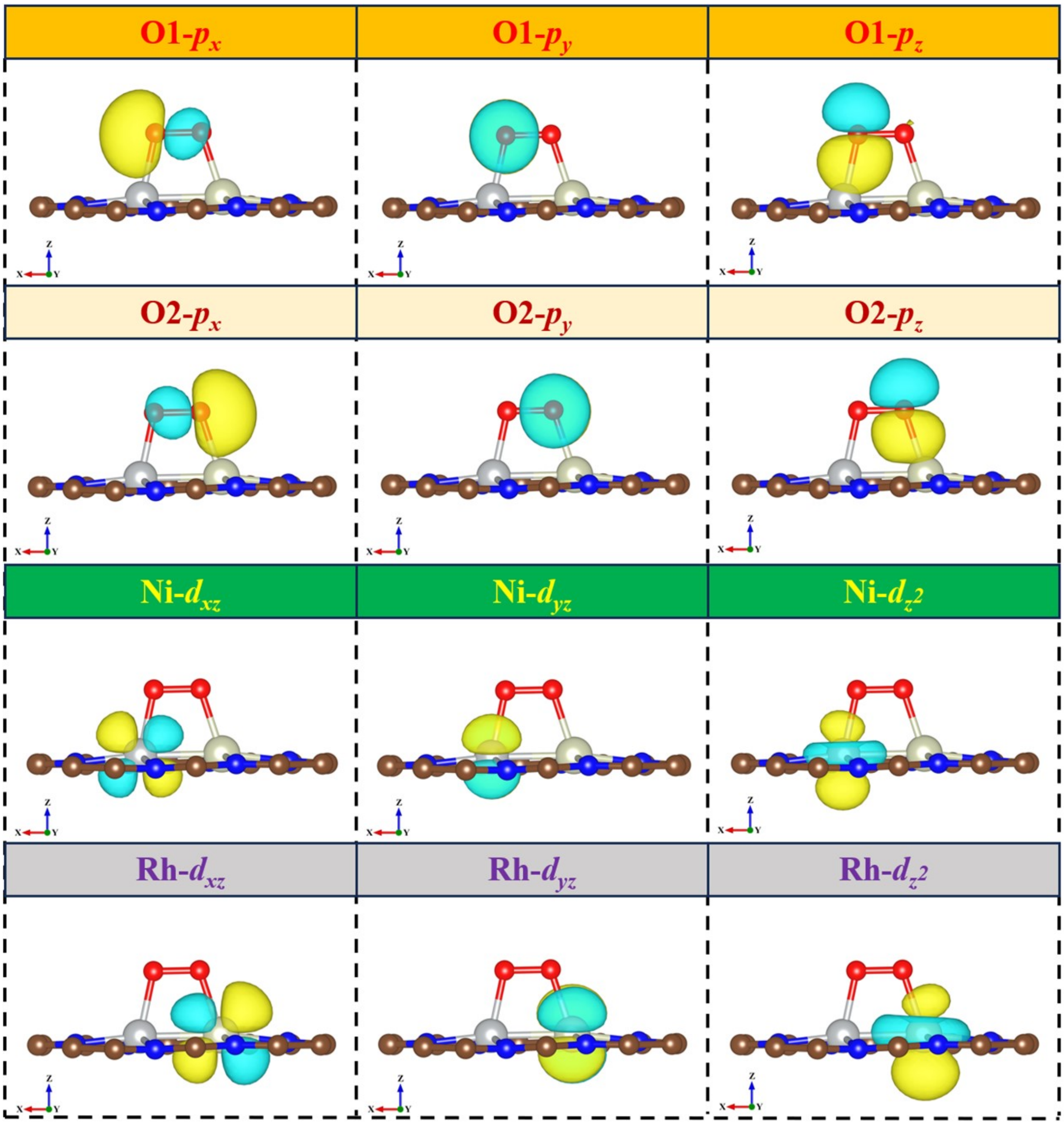

Figure S19 The d_{xz}, d_{yz}, d_{z^2} orbital Wannier function of Ni, Rh atom and the p_x, p_y, p_z orbital Wannier function of O1, O2 atom in NiRh-NDG&O_2.

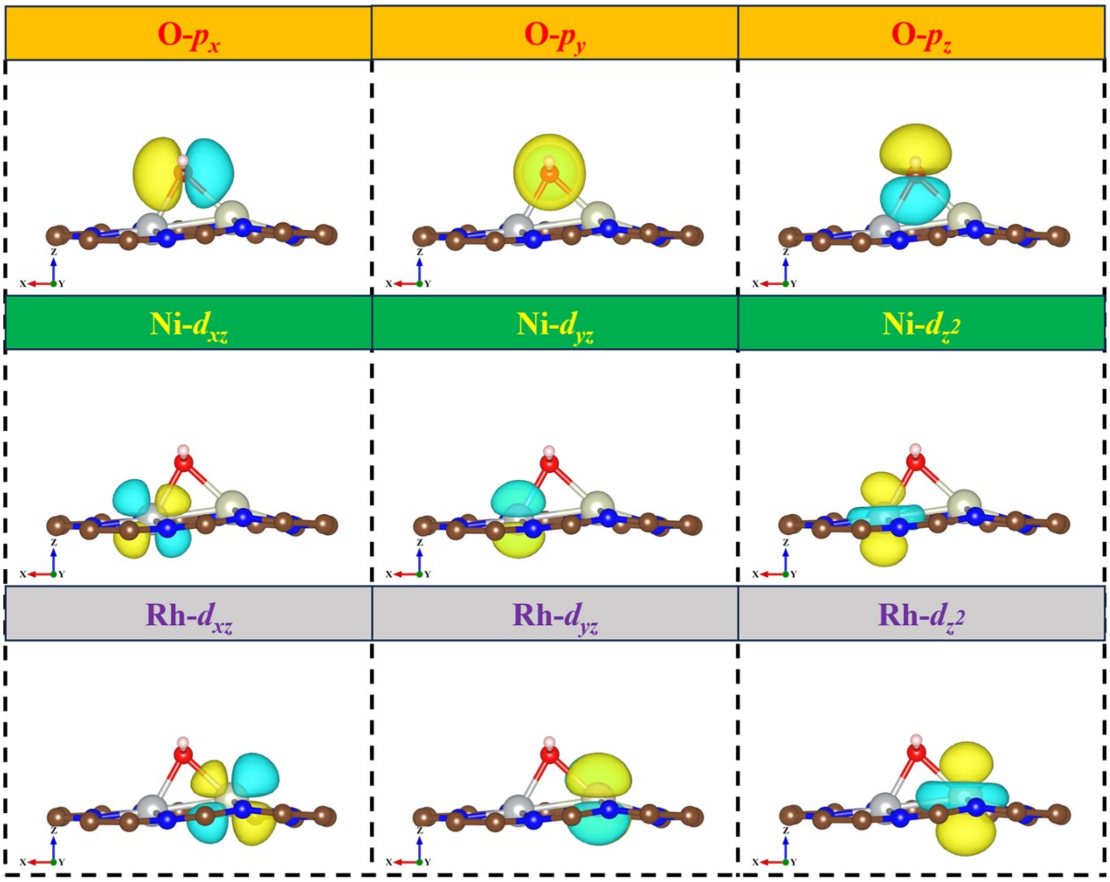

Figure S20 The d_{xz}, d_{yz}, d_{z^2} orbital Wannier function of Ni, Rh atom and the p_x, p_y, p_z orbital Wannier function of O atom in NiRh-NDG&OH.

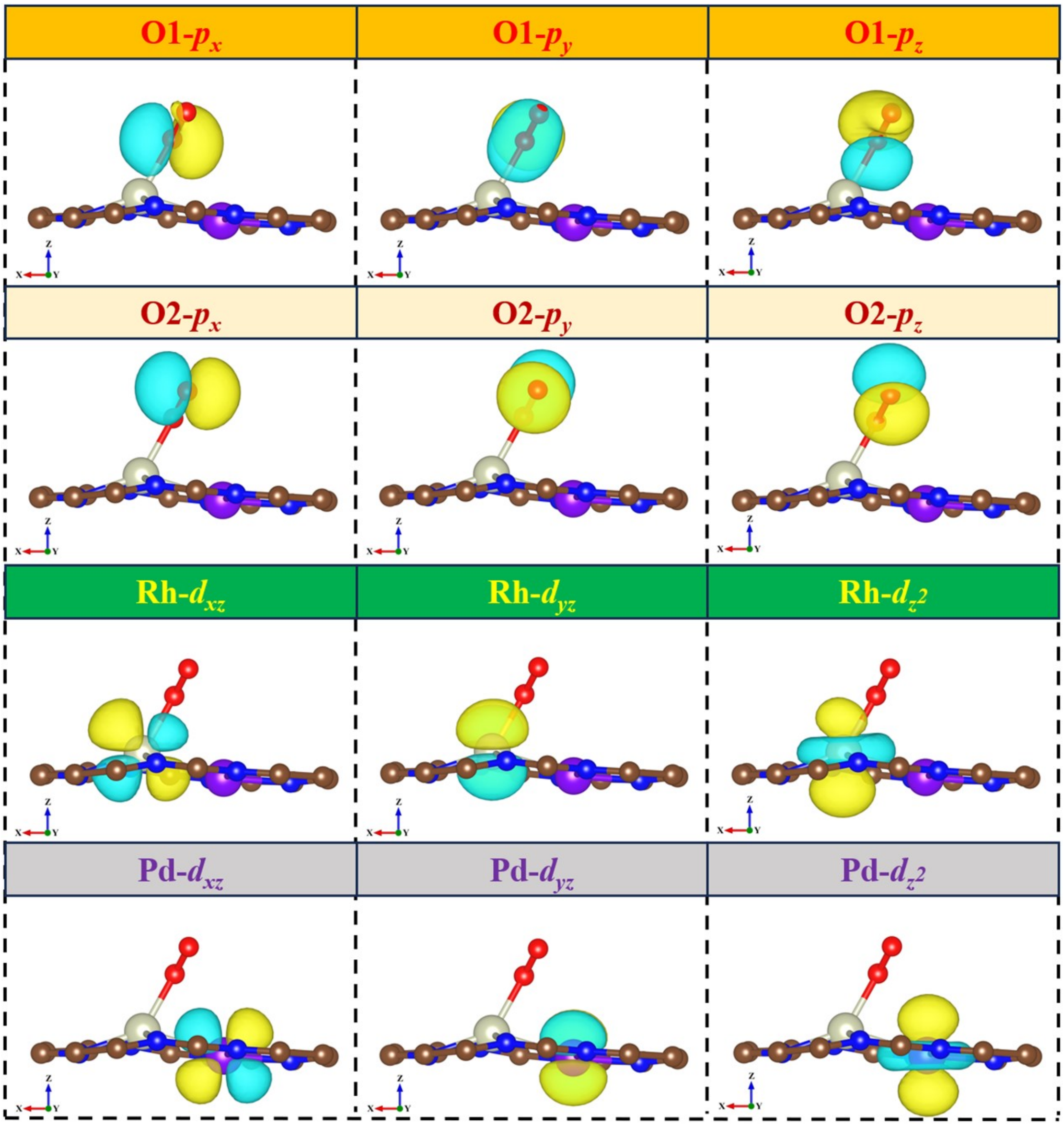

Figure S21 The d_{xz}, d_{yz}, d_{z^2} orbital Wannier function of Rh, Pd atom and the p_x, p_y, p_z orbital Wannier function of O1, O2 atom in RhPd-NDG&O_2.

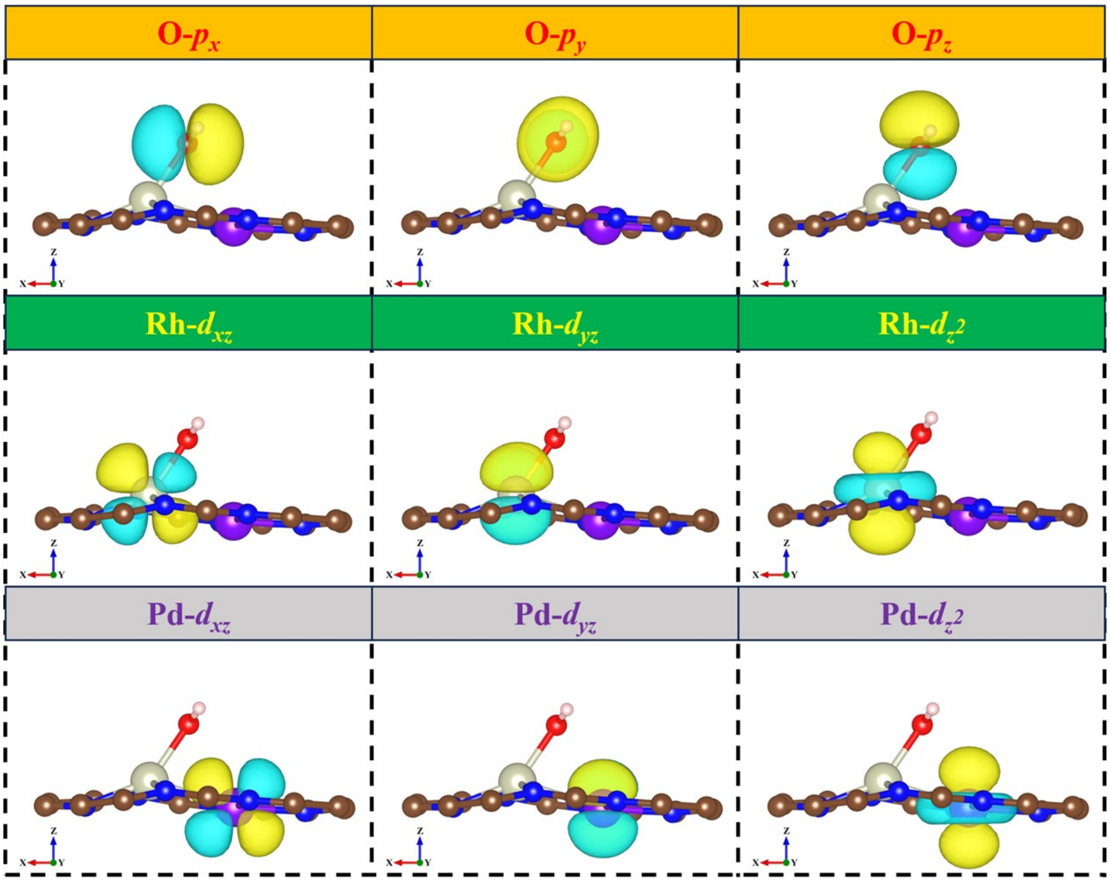

Figure S22 The d_{xz}, d_{yz}, d_{z^2} orbital Wannier function of Rh, Pd atom and the p_x, p_y, p_z orbital Wannier function of O atom in RhPd-NDG&OH.

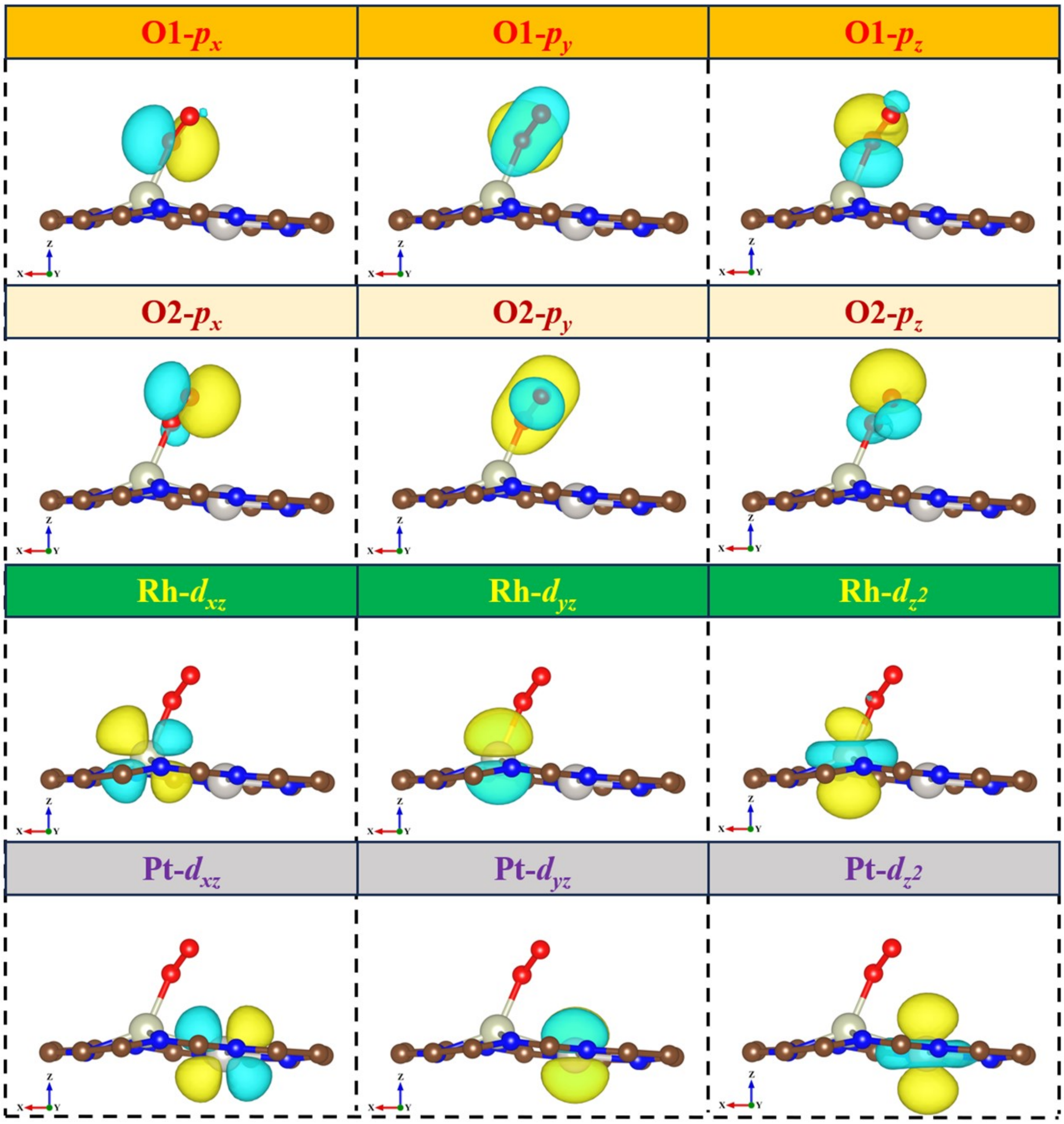

Figure S23 The d_{xz}, d_{yz}, d_{z^2} orbital Wannier function of Rh, Pt atom and the p_x, p_y, p_z orbital Wannier function of O1, O2 atom in RhPt-NDG&O_2.

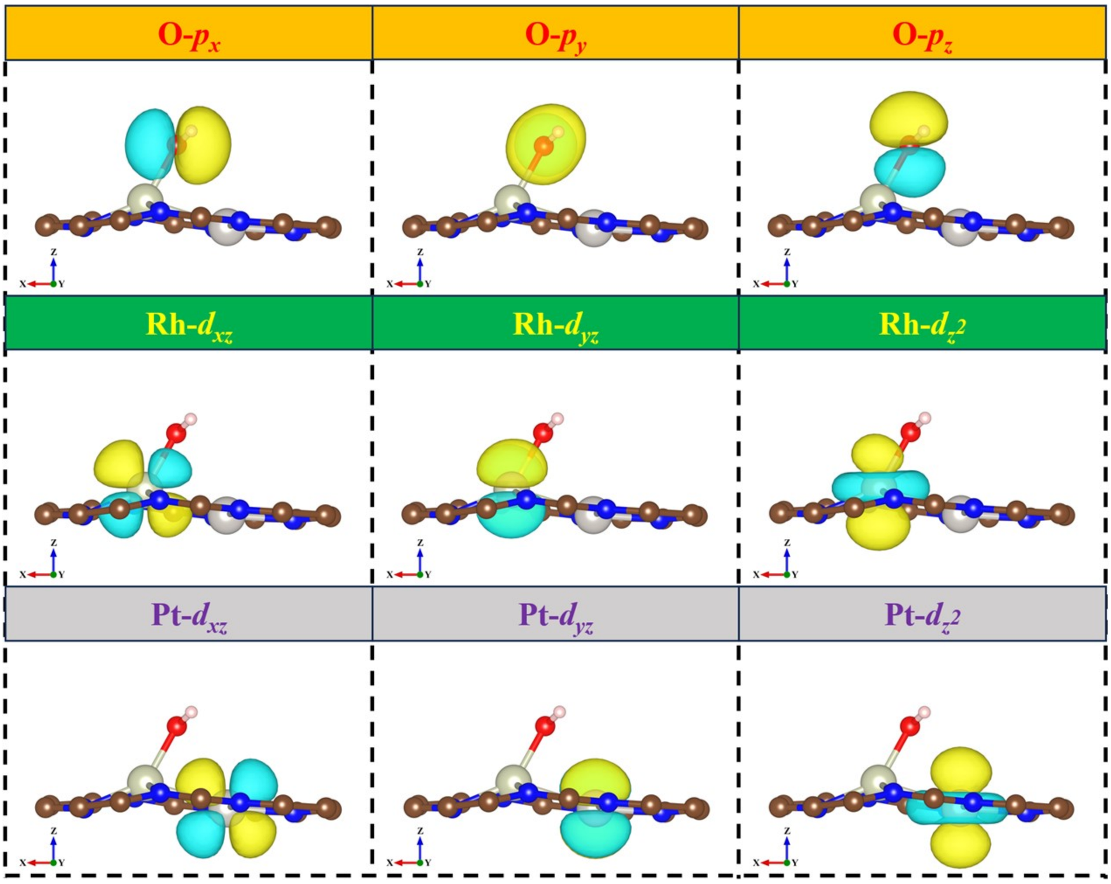

Figure S24 The d_{xz}, d_{yz}, d_{z^2} orbital Wannier function of Rh, Pt atom and the p_x, p_y, p_z orbital Wannier function of O atom in RhPt-NDG&OH.

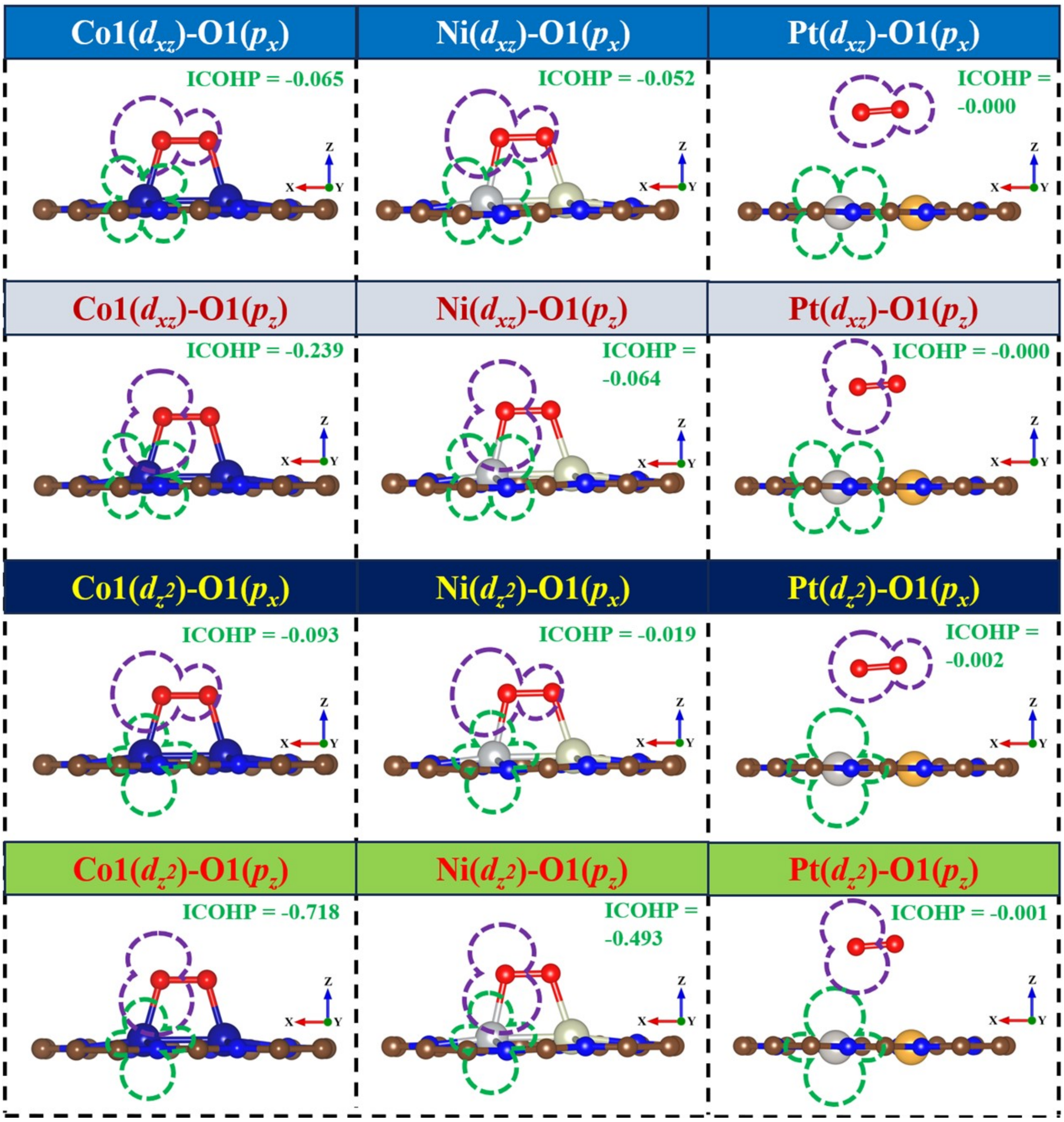

Figure S25 Orbital coupling diagram of M_1(*d*)-O1(*p*) in CoCo-NDG&O_2, NiRh-NDG&O_2, PtAu-NDG&O_2 (The purple dashed line indicates the *p* orbitals Wannier function profile of O1 atom, where the green dashed line indicates the *d* orbitals Wannier function profile of M_1 atom, and the green ICOHP indicates the bond strength of the corresponding orbital coupling between M_1 and O1 atom).

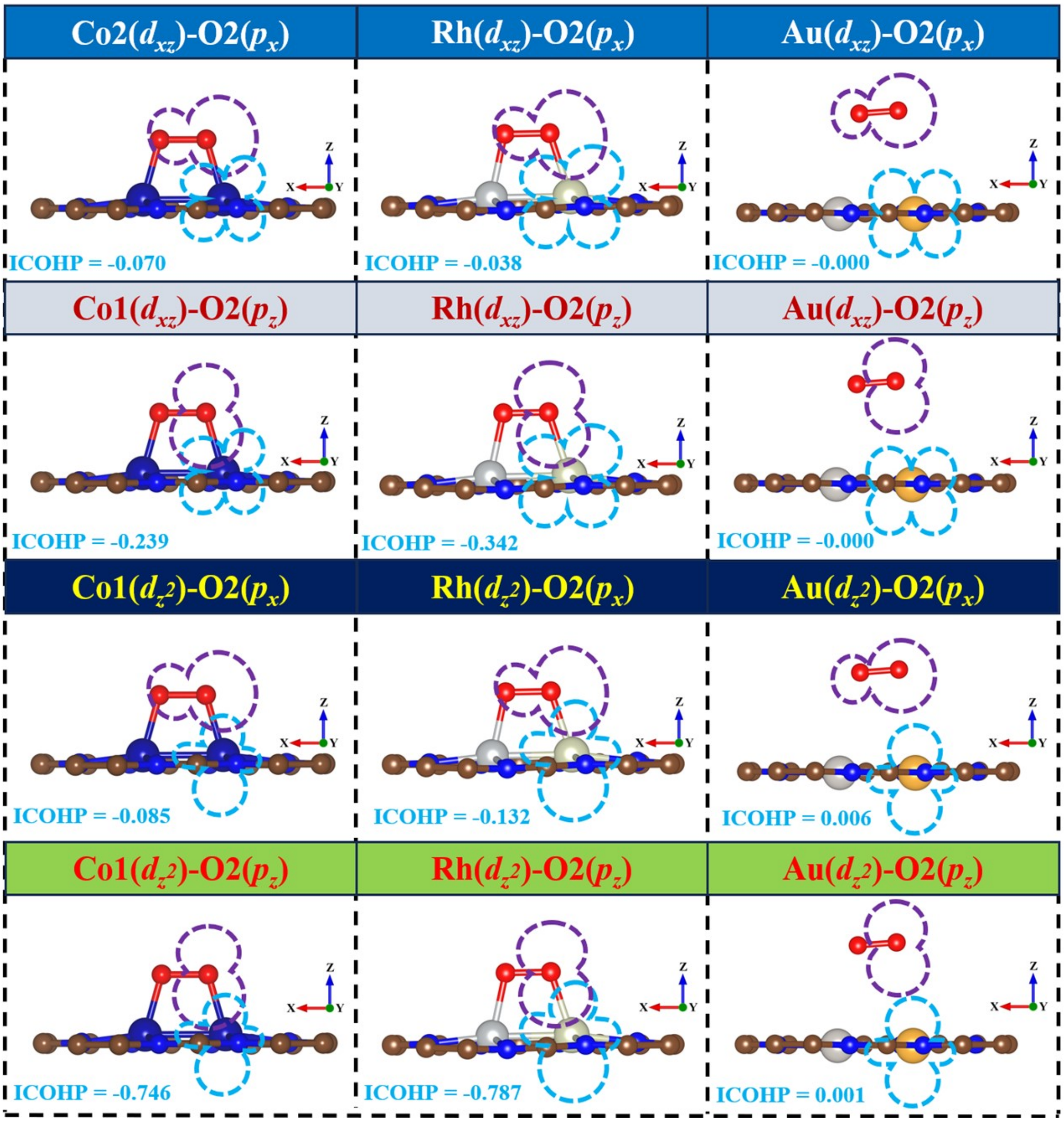

Figure S26 Orbital coupling diagram of M_2(*d*)-O2(*p*) in CoCo-NDG&O_2, NiRh-NDG&O_2, PtAu-NDG&O_2 (The purple dashed line indicates the *p* orbital Wannier function profile of O2 atom, where the green dashed line indicates the *d* orbital Wannier function profile of M_2 atom, and the green ICOHP indicates the bond strength of the corresponding orbital coupling between M_2 and O2 atom).

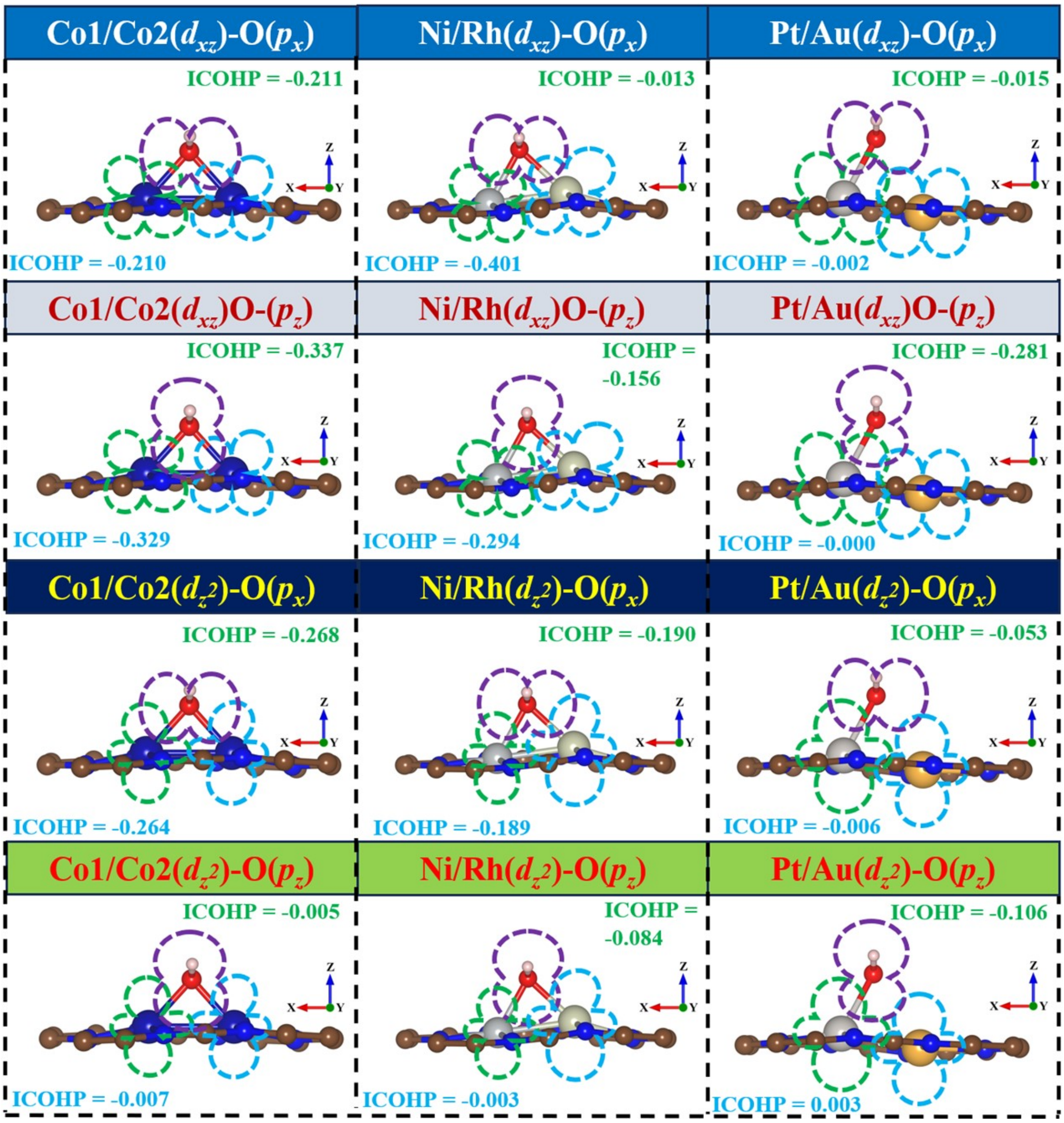

Figure S27 Orbital coupling diagram of $M_1/M_2(d)$-O(p) in CoCo-NDG&OH, NiRh-NDG&OH, PtAu-NDG&OH (The purple dashed line indicates the p orbitals Wannier function profile of O atom, where the green/blue dashed line indicates the d orbitals Wannier function profile of M_1/M_2 atom, and the green/blue ICOHP indicates the bond strength of the corresponding orbital coupling between M_1/M_2 and O atom).

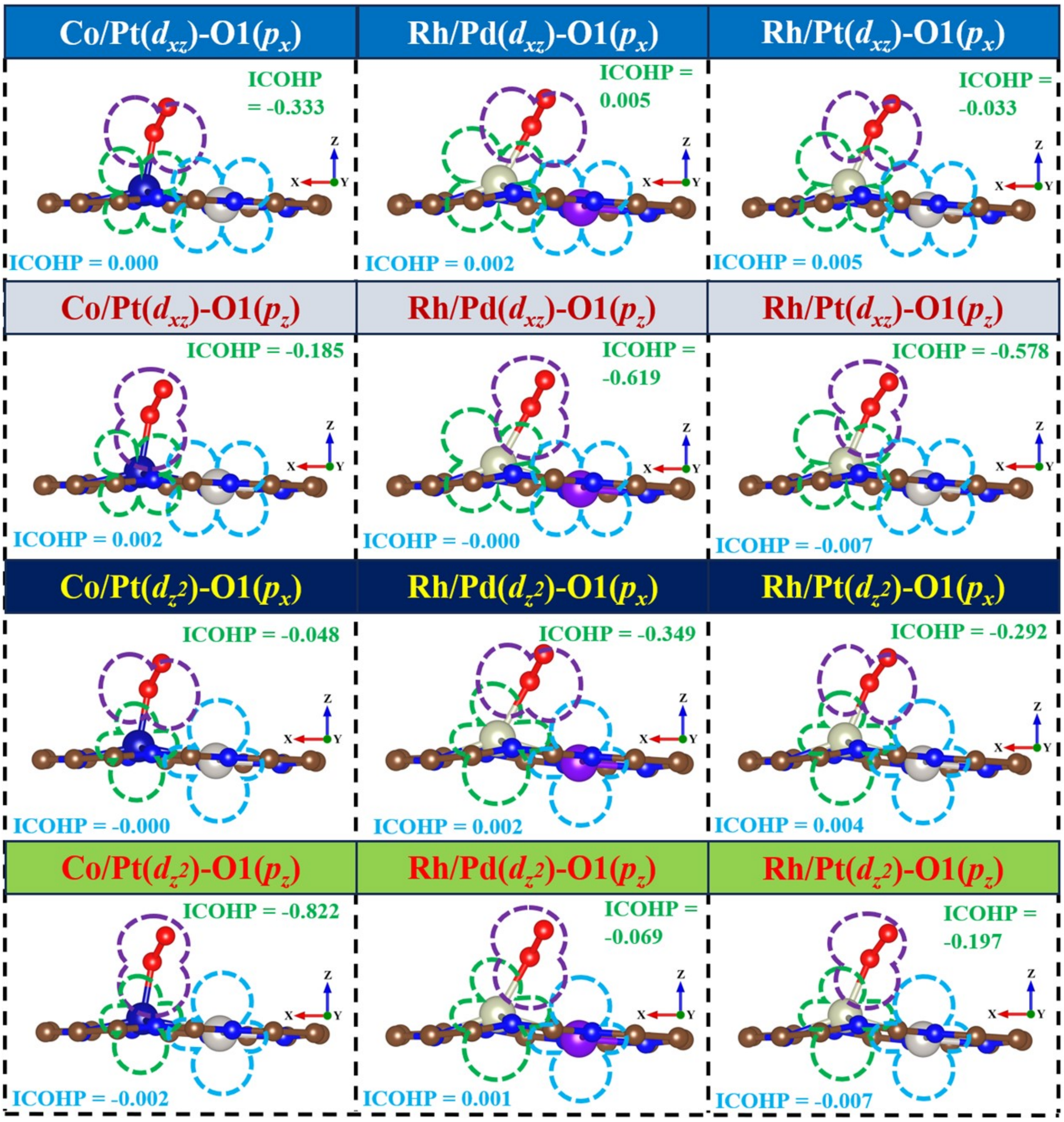

Figure S28 Orbital coupling diagram of M$_1$(*d*)-O1(*p*) in CoPt-NDG&O$_2$, RhPd-NDG&O$_2$, RhPt-NDG&O$_2$ (The purple dashed line indicates the *p* orbitals Wannier function profile of O1 atom, where the green/blue dashed line indicates the *d* orbitals Wannier function profile of M$_1$/M$_2$ atom, and the green/blue ICOHP indicates the bond strength of the corresponding orbital coupling between M$_1$/M$_2$ and O1 atom).

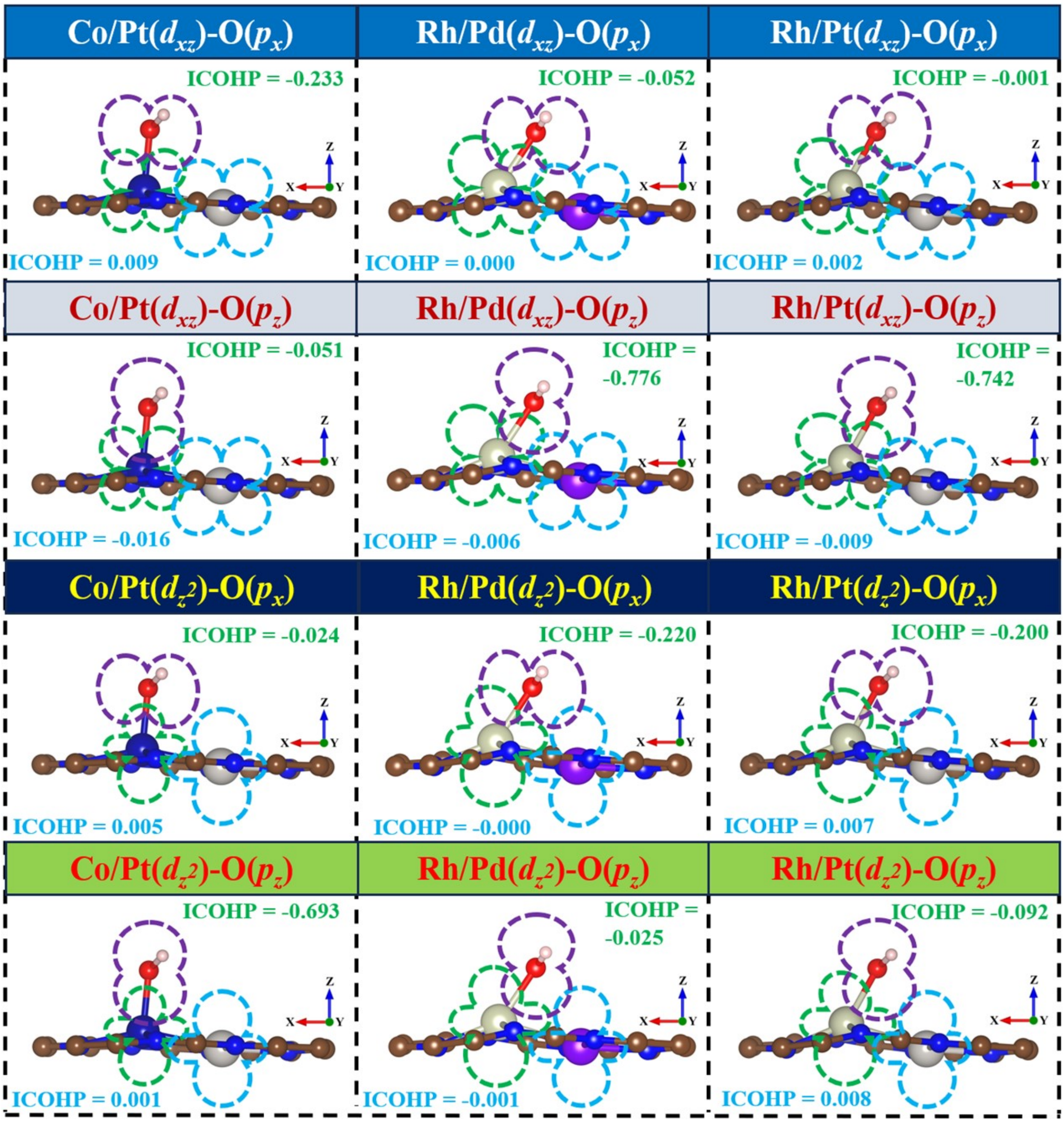

Figure S29 Orbital coupling diagram of M_1(*d*)-O(*p*) in CoPt-NDG&OH, RhPd-NDG&OH, RhPt-NDG&OH (The purple dashed line indicates the *p* orbitals Wannier function profile of O atom, where the green/blue dashed line indicates the *d* orbitals Wannier function profile of M_1/M_2 atom, and the green/blue ICOHP indicates the bond strength of the corresponding orbital coupling between M_1/M_2 and O atom).

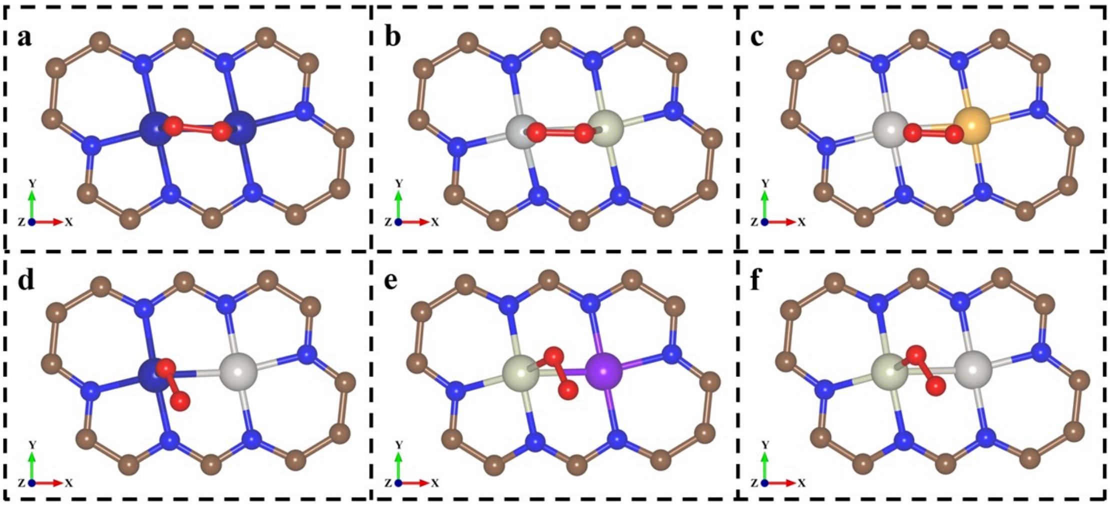

Figure S30 Top view of a. CoCo-NDG&O_2, b. NiRh-NDG&O_2, c. PtAu-NDG, d. CoPt-NDG&O_2, e. RhPd-NDG&O_2, and f. RhPt-NDG&O_2.

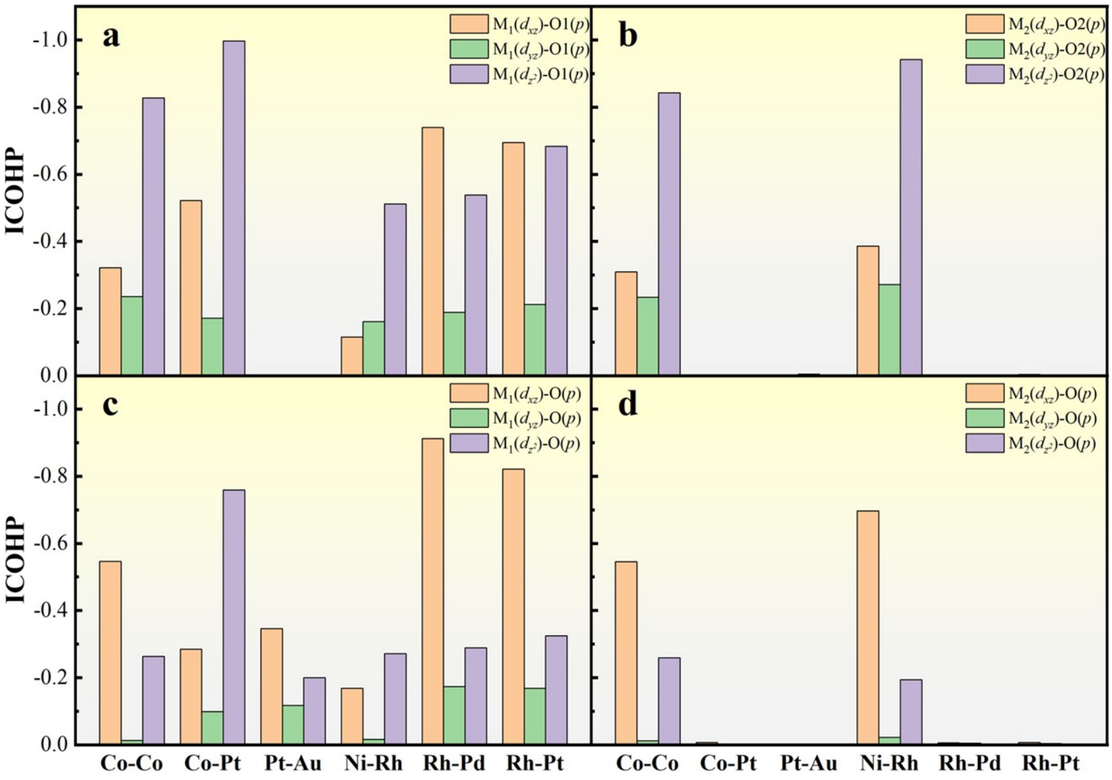

Figure S31 Contribution of different orbital couplings in M_1M_2-NDG&O_2 to a. $M_1(d)$-$O(p)$ and b. $M_2(d)$-$O(p)$; Contribution of different orbital couplings in M_1M_2-NDG&OH to c. $M_1(d)$-$O(p)$ and d. $M_2(d)$-$O(p)$.

Note S10 Contribution of different orbital couplings to the M-O bond:

Previous studies have suggested for the M-N-C structure[7,14], only the atomic orbitals in the Z-axis direction of the metal atoms may be involved in the bonding of the intermediate species, so we have only considered the d_{xz}, d_{yz}, d_{z^2} orbital on the M_1, M_2 atom.

As shown in **Fig. S31**, it is not difficult to see that the coupling of the d_{xz} or d_{z^2} orbital to the p orbitals (p_x, p_y, p_z) plays a dominant role in the bonding between M_1/M_2 atom and O atom in both $^*O_2$ and *OH, and there is even a case of synergistic regulation of bonding between the two. However, the contribution of d_{yz} orbital to bonding is much smaller than that of the first two in the overall view, which is likely to be caused by the fact that d_{yz} orbital are less occupied by electrons near the Fermi level of the six systems, and their own spatial structure is unfavorable to match with p orbitals of O atom. Therefore, the bonding mechanism between d_{yz} and p orbitals is not discussed in detail in this paper.

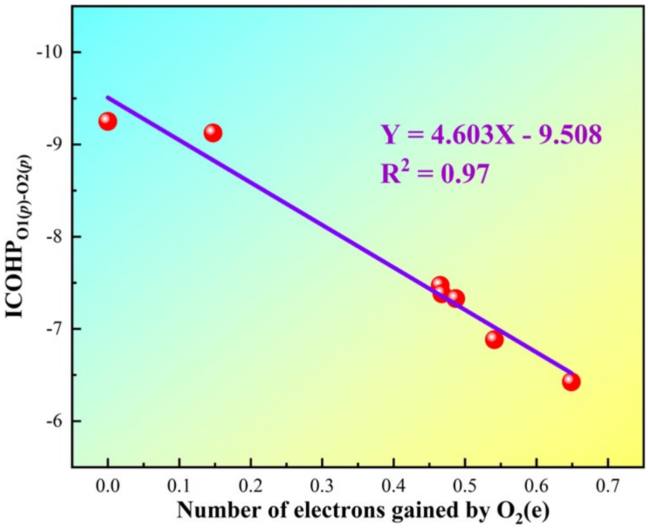

Figure S32 Linear fit between the number of electrons gained by O_2 and $\mathrm{ICOHP}_{O1(p)\text{-}O2\text{-}(p)}$.

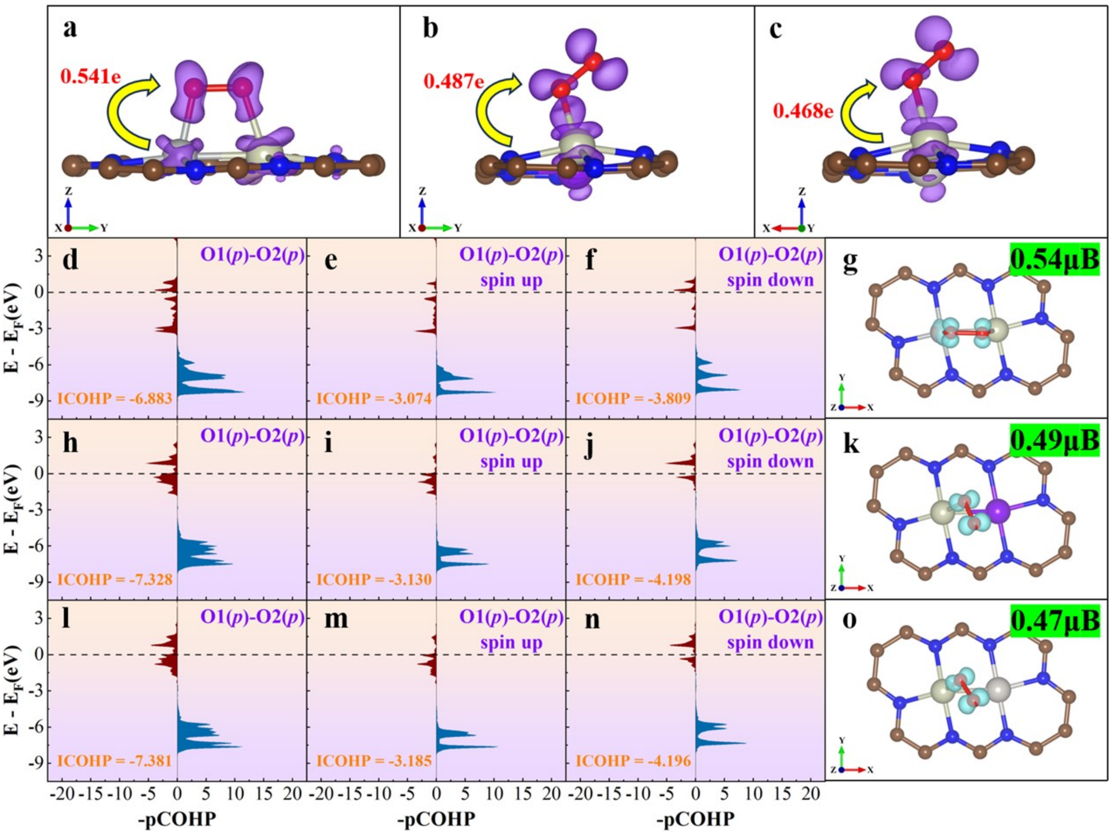

Figure S33 Charge density difference of a. NiRh-NDG, b. RhPd-NDG, c. RhPt-NDG (only the part of electrons gained is included, and the isosurface is set to 0.05e/Bohr^3); pCOHP of the d. O1(*p*)-O2(*p*), e. spin-up O1(*p*)-O2(*p*), f. spin-down O1(*p*)-O2(*p*) on NiRh-NDG&O_2, g. the spin density of O_2 in NiRh-NDG&O_2; pCOHP of the h. O1(*p*)-O2(*p*), i. spin-up O1(*p*)-O2(*p*), j. spin-down O1(*p*)-O2(*p*) on RhPd-NDG&O_2, k. the spin density of O_2 in RhPd-NDG&O_2; pCOHP of the l. O1(*p*)-O2(*p*), m. spin-up O1(*p*)-O2(*p*), n. spin-down O1(*p*)-O2(*p*) on RhPt-NDG&O_2, o. the spin density of O_2 in RhPt-NDG&O_2.

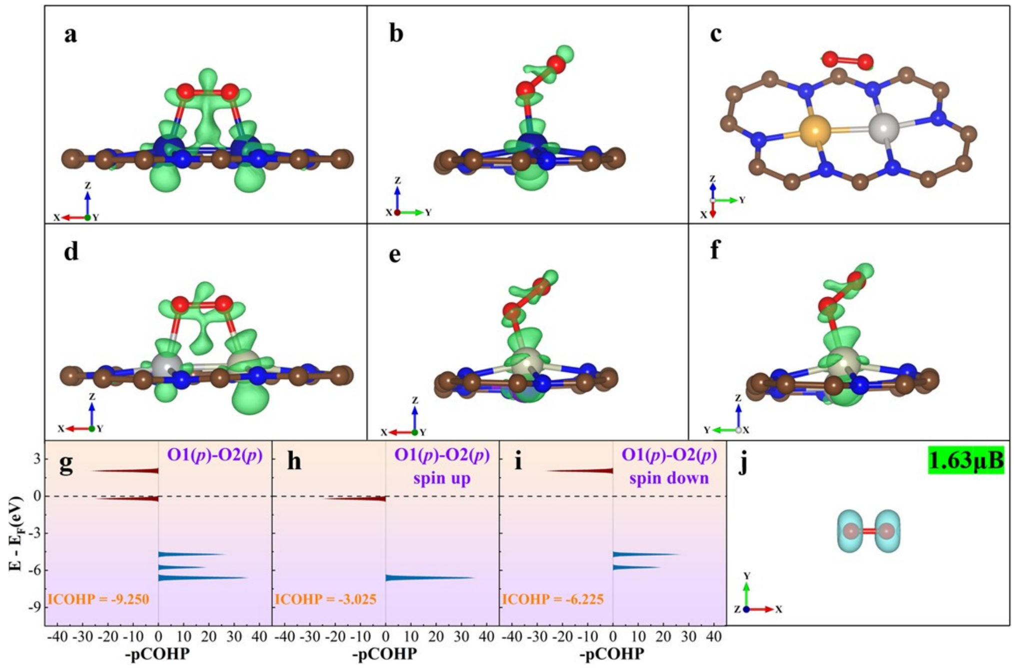

Figure S34 Charge density difference of a. CoCo-NDG, b. CoPt-NDG, c. PtAu-NDG, d. NiRh-NDG, e. RhPd-NDG, and f. RhPt-NDG (Only the part of electrons loss is included, the isosurface is set to 0.05e/Bohr^3); pCOHP of the g. O1(*p*)-O2(*p*), h. spin-up O1(*p*)-O2(*p*), i. spin-down O1(*p*)-O2(*p*) on pure O_2, and j. the spin density of pure O_2.

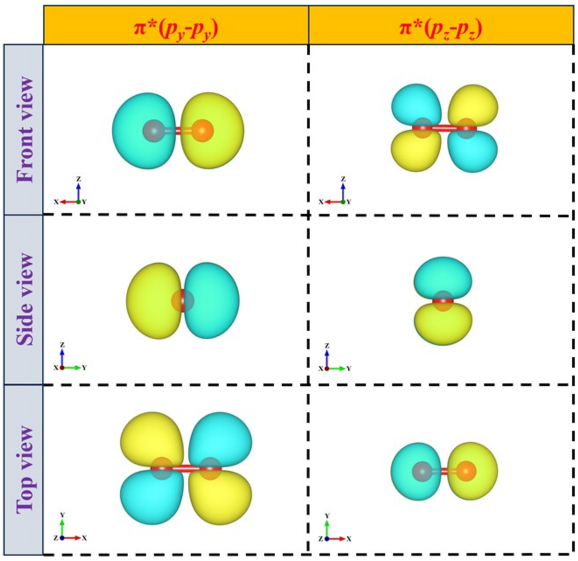

Figure S35 Front, side, and top views of π* orbital Wannier function of pure O_2 (When O_2 is parallel to the X/Y axis, the π* orbital consists of the p_y/p_x orbital and p_z orbital of the O1, O2 atom, and p_x/p_y orbital will form σ orbitals).

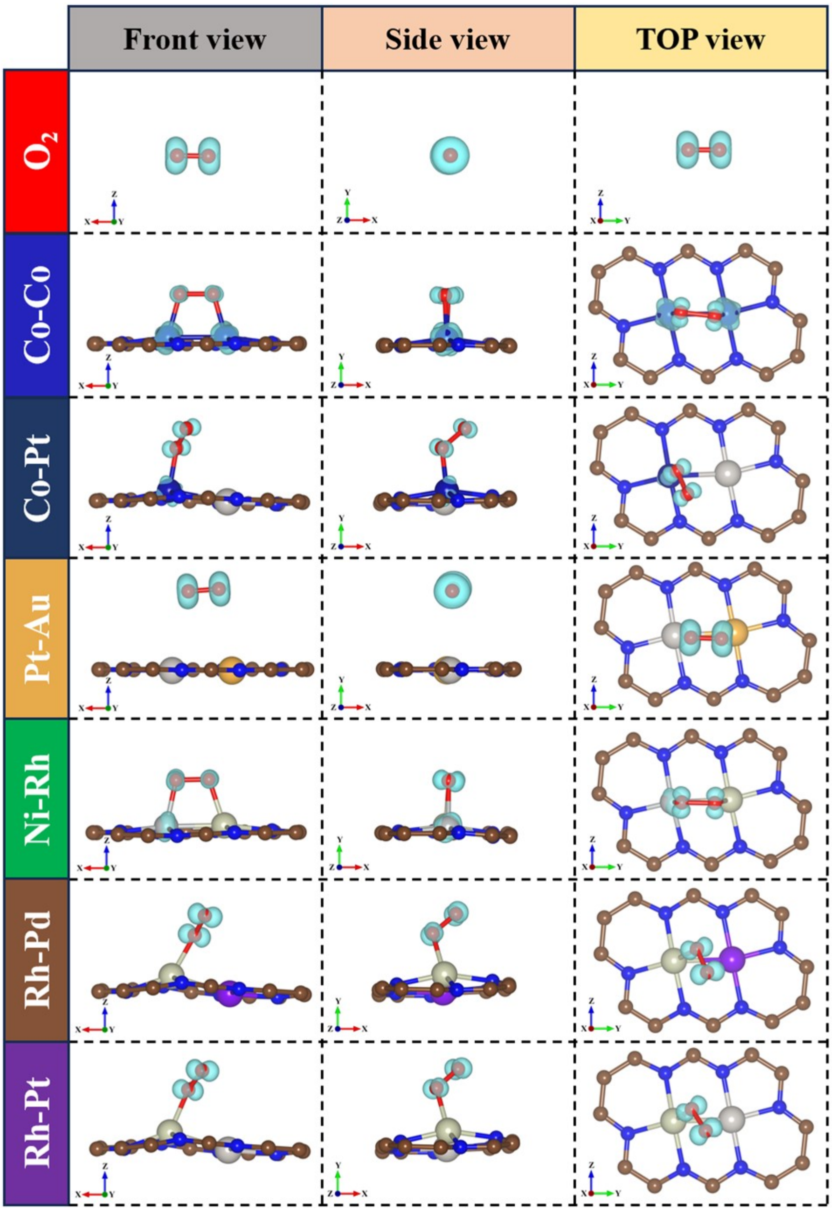

Figure S36 Front, side, and top view of the spin density of pure O_2, CoCo-NDG&O_2, CoPt-NDG&O_2, PtAu-NDG&O_2, NiRh-NDG&O_2, RhPd-NDG&O_2, and RhPt-NDG&O_2.

Note S11 Magnetic moment analysis:

Notice that in the Charge density difference diagrams (**Fig. S34a~f**), the electrons in the d_{z^2} orbital of the M_1, M_2 atom are significantly reduced (**Fig. S36**). Combined with the previous analyses, the M(d_{z^2})-(p_z) or M(d_{xz})-O(p_z) in the bonding of M_1/M_2

atom to O1/O2 atom is a major contributor, which suggests the electrons in the d_{z^2} or d_{xz} orbital of the M_1/M_2 atom are transferred to the p_z orbital of the O1/O2 atom and are paired with the unpaired free electrons in the p_z orbital, resulting in a significant decrease in the Z-axis magnetic moment of O_2. However, the coupling of M_1 and M_2 atom to the p_x or p_y orbital of O1 and O2 atom is not a dominant form of bonding, so that relatively few electrons are supplied to the p_x and p_y orbitals, thus retaining a certain amount of magnetic moment in the X-axis and Y-axis direction (**Fig. S36**).

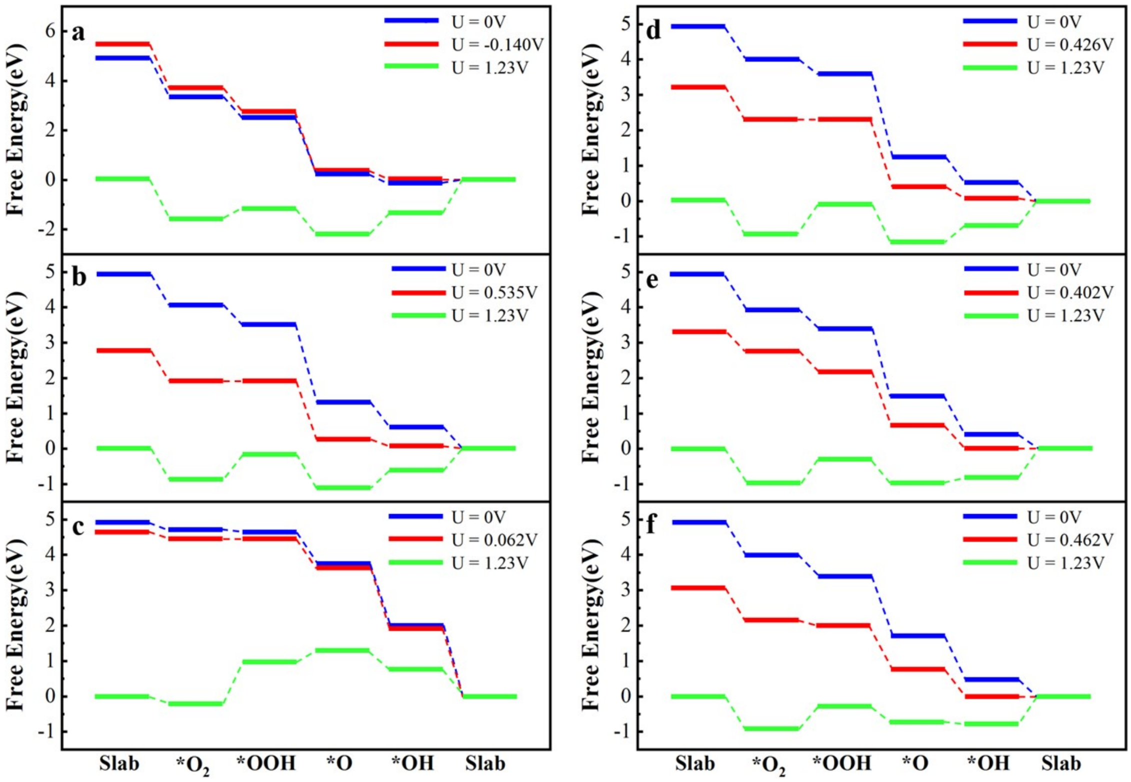

Figure S37 Free energy profile of ORR on a. CoCo-NDG, b. CoPt-NDG, c. PtAu-NDG, d. NiRh-NDG, e. RhPd-NDG, and f. RhPt-NDG at different applied potentials (Blue line denotes the applied potential of 0 V, red line denotes the limiting potential (the minimum potential at which the reaction can proceed spontaneously)[15], and green line denotes the applied potential of 1.23V).

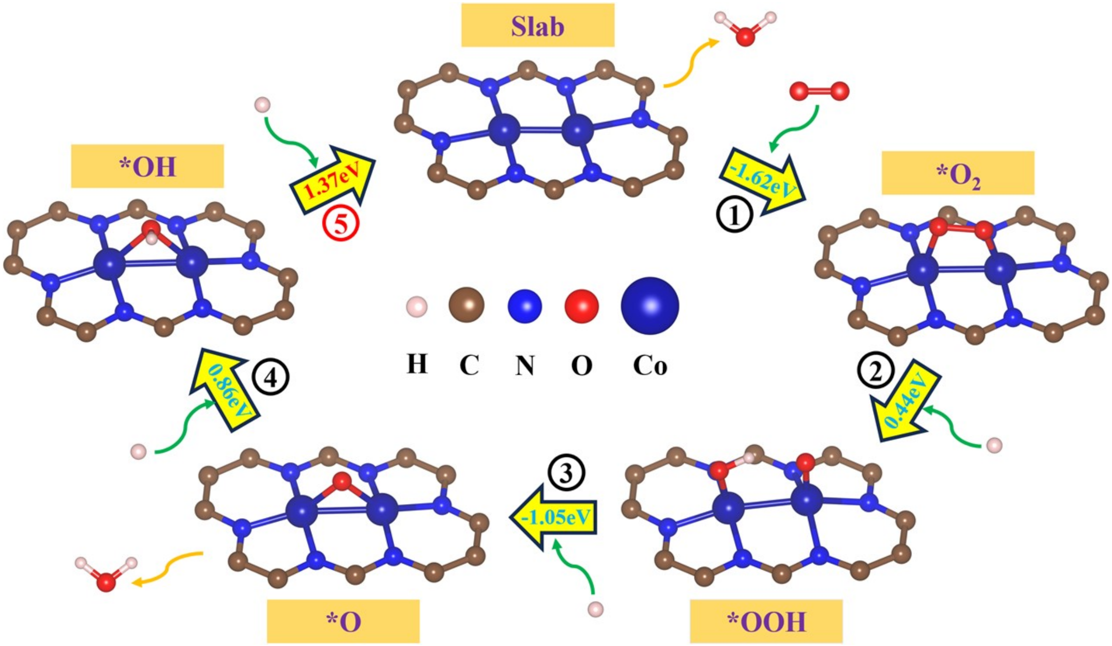

Figure S38 Flow diagram of ORR pathway on CoCo-NDG (U = 1.23V, the red circles indicate PDS).

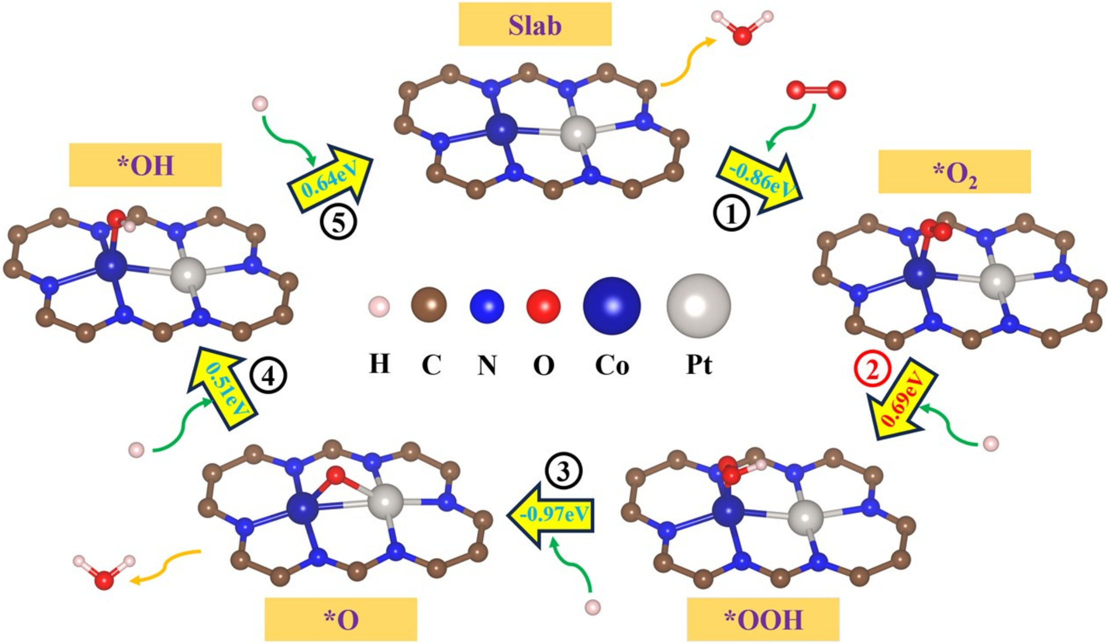

Figure S39 Flow diagram of ORR pathway on CoPt-NDG (U = 1.23V, the red circles indicate PDS).

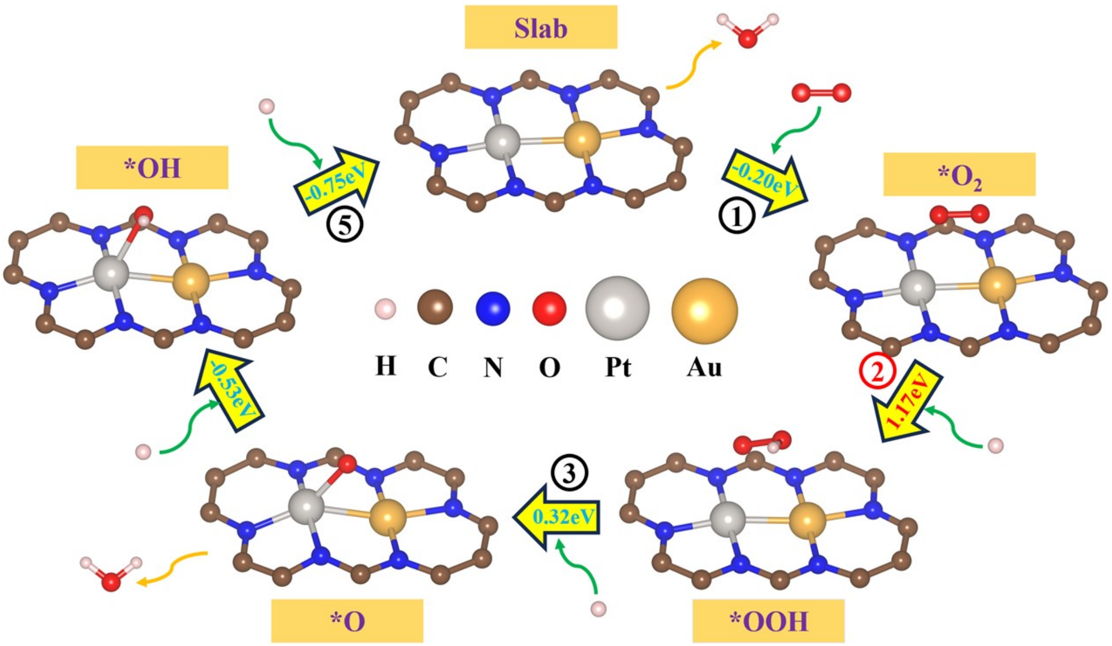

Figure S40 Flow diagram of ORR pathway on PtAu-NDG (U = 1.23V, the red circles indicate PDS).

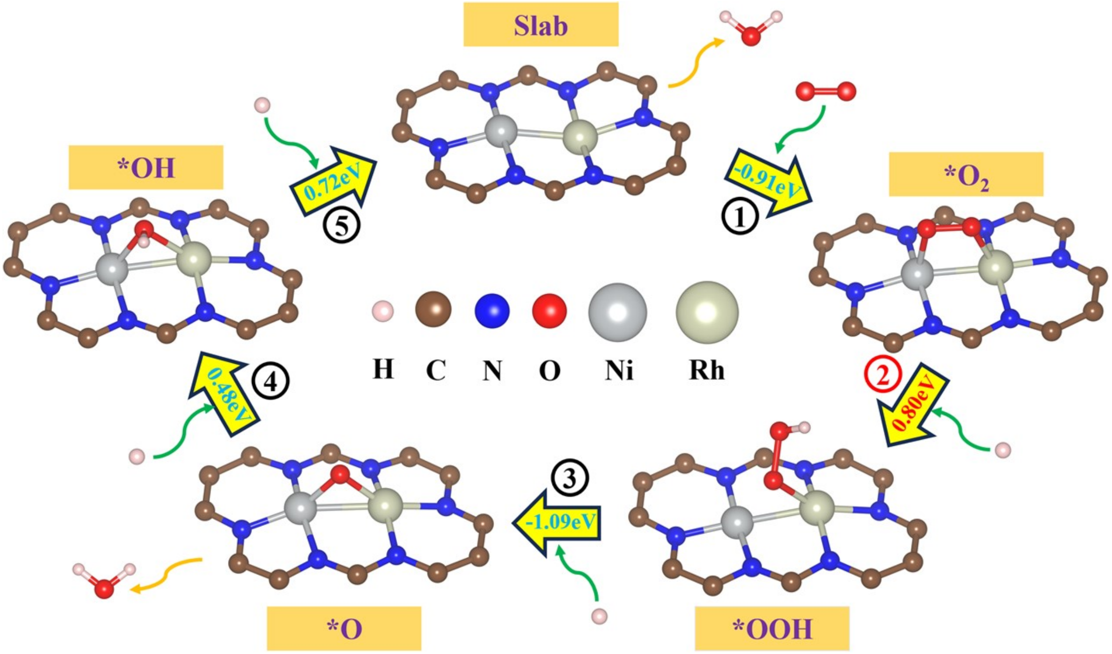

Figure S41 Flow diagram of ORR pathway on NiRh-NDG (U = 1.23V, the red circles indicate PDS).

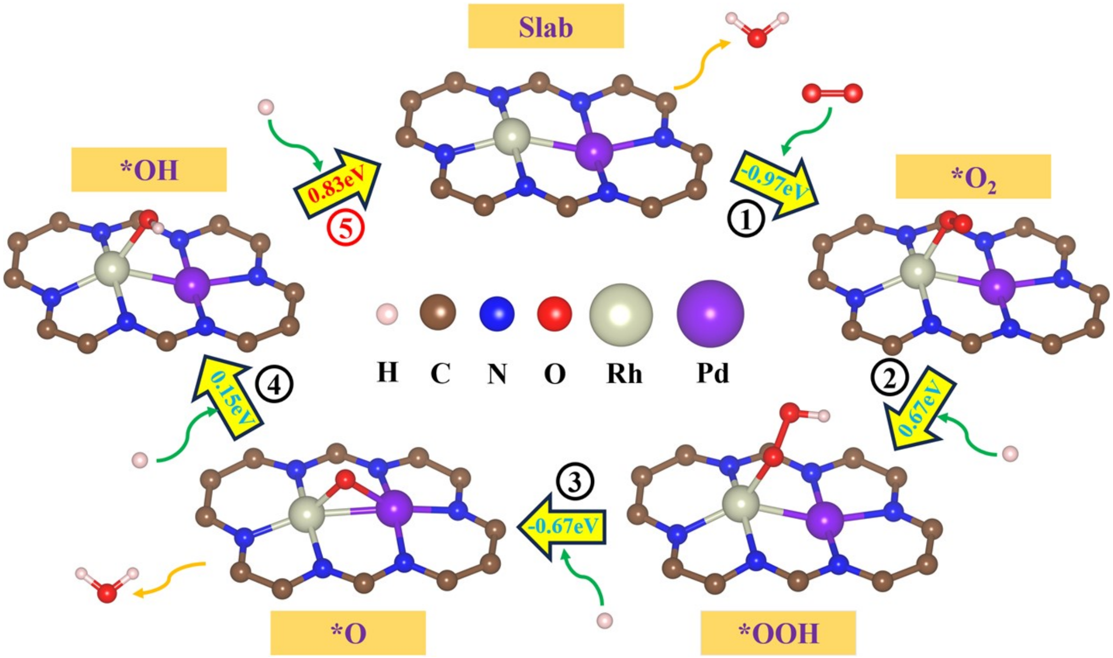

Figure S42 Flow diagram of ORR pathway on RhPd-NDG (U = 1.23V, red circles indicate PDS).

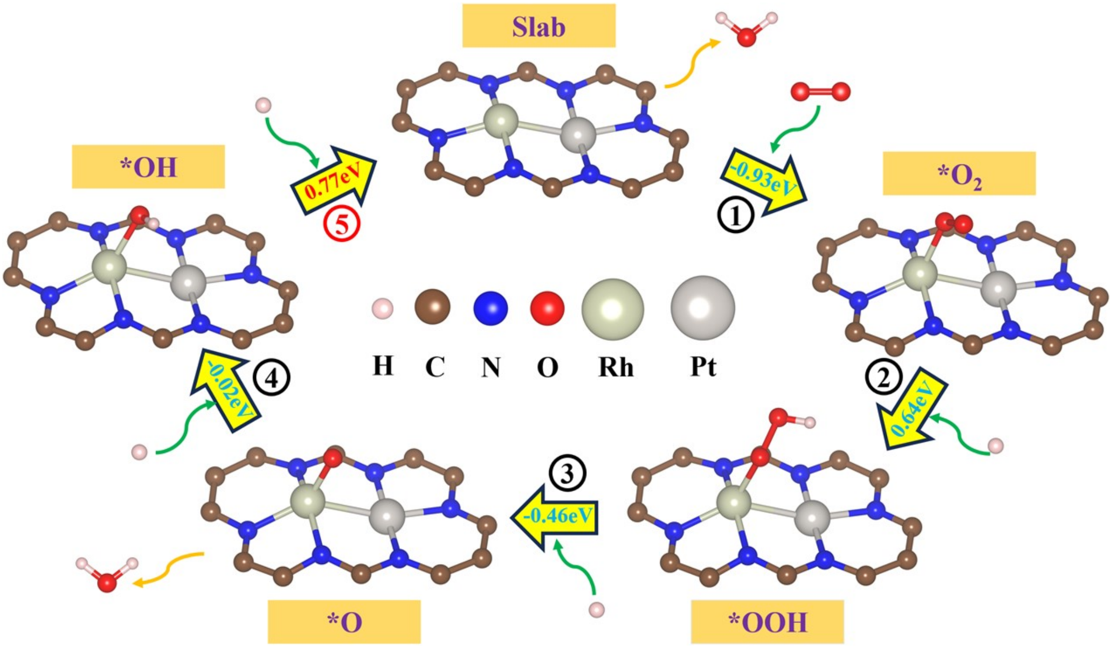

Figure S43 Flow diagram of ORR pathway on RhPt-NDG (U = 1.23V, red circles indicate PDS).

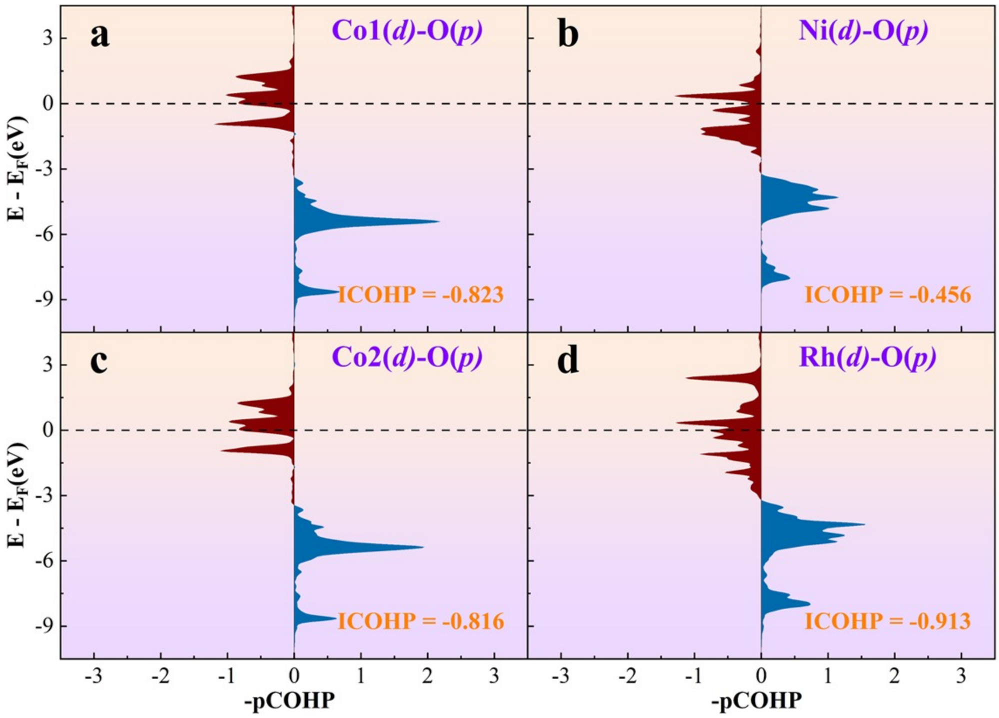

Figure S44 pCOHP of a. Co1(*d*)-O(*p*) in CoCo-NDG&OH, b. Ni(*d*)-O(*p*) in NiRh-NDG&OH, c. Co2(*d*)-O(*p*) in CoCo-NDG&OH, and d. Rh(*d*)-O(*p*) in NiRh-NDG&OH.

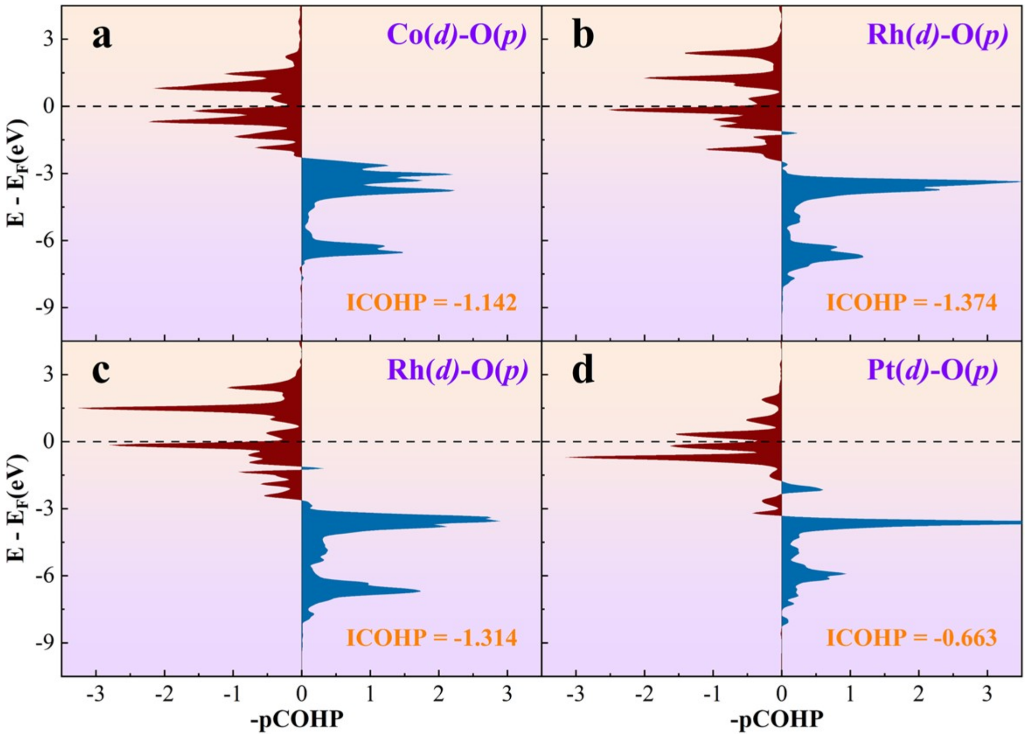

Figure S45 pCOHP of the a. Co(*d*)-O(*p*) in CoPt-NDG&OH, b. Rh(*d*)-O(*p*) in RhPd-NDG&OH, c. Rh(*d*)-O(*p*) in RhPt-NDG&OH, and d. Pt(*d*)-O(*p*) in PtAu-NDG&OH.

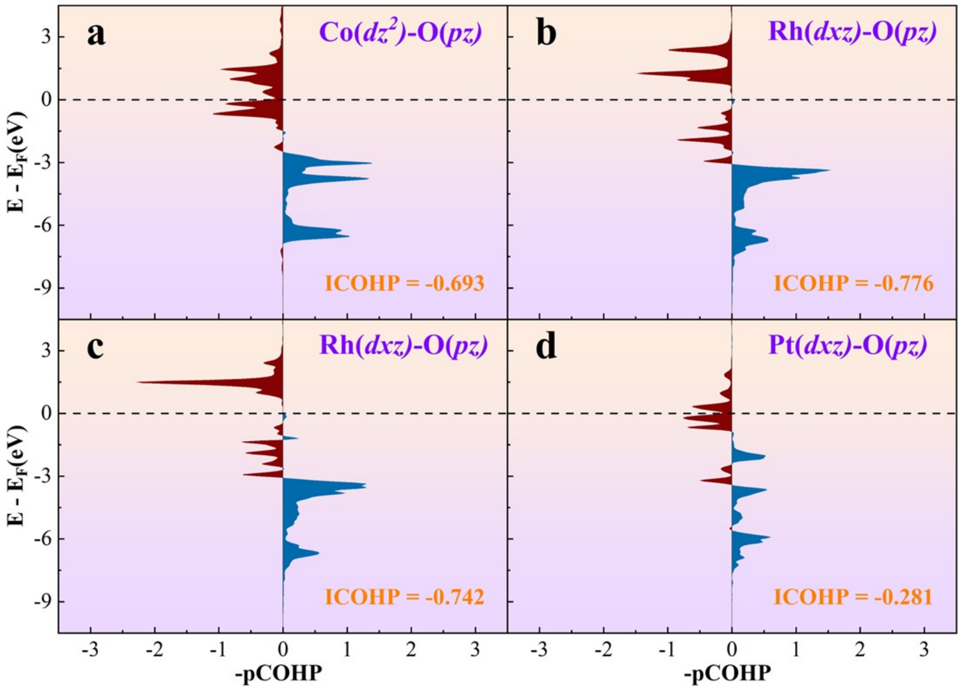

Figure S46 pCOHP of a. Co(d_{z^2})-O(p_z) in CoPt-NDG&OH, b. Rh(d_{xz})-O(p_z) in RhPd-NDG&OH, c. Rh(d_{xz})-O(p_z) in RhPt-NDG&OH, and d. Pt(d_{xz})-O(p_z) in PtAu-NDG&OH.

Note S12 Synergistic orbital coupling mechanisms in other catalytic reactions, and applications to experimental studies:

Firstly, we take Nitrogen reduction reaction (NRR) as an example, N_2 takes the Side-on mode on CoCo-NDG and NiRh-NDG (**Fig. S47a** and **Fig. S48a**), while it takes the End-on mode on CoPt-NDG, RhPd-NDG, RhPt-NDG (**Fig. S47b** and **Fig. S48b, c**), and Physisorption mode on PtAu-NDG (**Fig. S47c**), and it can be seen that the adsorption mode of N_2 is the same as that of O_2 in the main text mode corresponds exactly to that of O_2 in the main text. As for Hydrogen evolution reaction (HER), CoCo-NDG, CoPt-NDG, NiRh-NDG adopted the Double-Bridge mode (**Fig. S47d, e** and **Fig.**

S48d), while PtAu-NDG, RhPd-NDG, RhPt-NDG adopted the Single-Bridge mode (**Fig. S47e** and **Fig. S48e, f**), which is very similar to our OH results. However, the difference between the adsorption mode of CoPt-NDG at *OH and *H is most likely caused by the d_{xz} orbital of the Pt atom having a small number of electrons at the Fermi level (**Fig. S47k**).

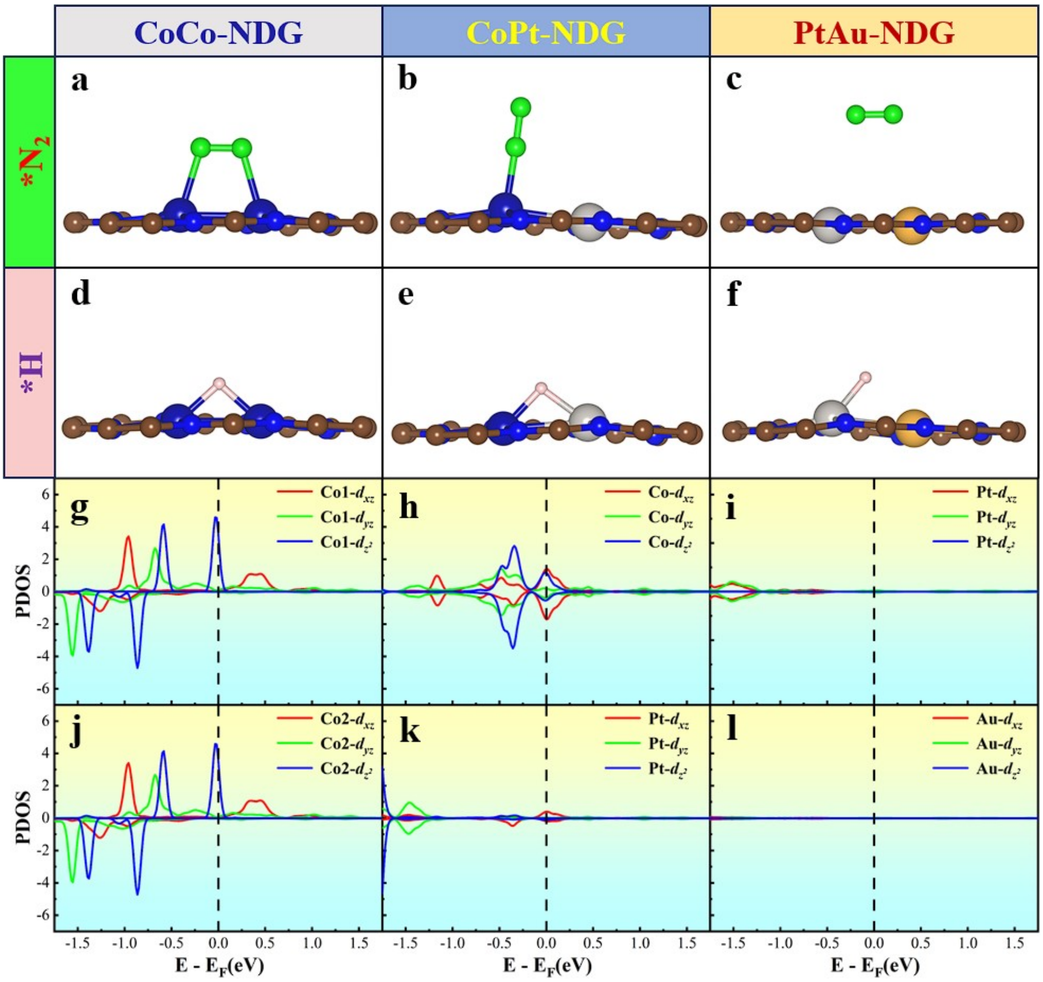

Figure S47 Front view of a. CoCo-NDG&N_2, b. CoPt-NDG&N_2, and c. PtAu-NDG&N_2; d. CoCo-NDG&H, e. CoPt-NDG&H, and f. PtAu-NDG&H; the d_{xz}, d_{yz}, d_{z^2} orbital DOS near Fermi level of M_1 atom in g. CoCo-NDG, h. CoPt-NDG, and i. PtAu-NDG; the d_{xz}, d_{yz}, d_{z^2} orbital DOS near the Fermi level of M_2 atom in j. CoCo-NDG, k. CoPt-NDG, and l. PtAu-NDG (Green atom indicate nitrogen atom in N_2).

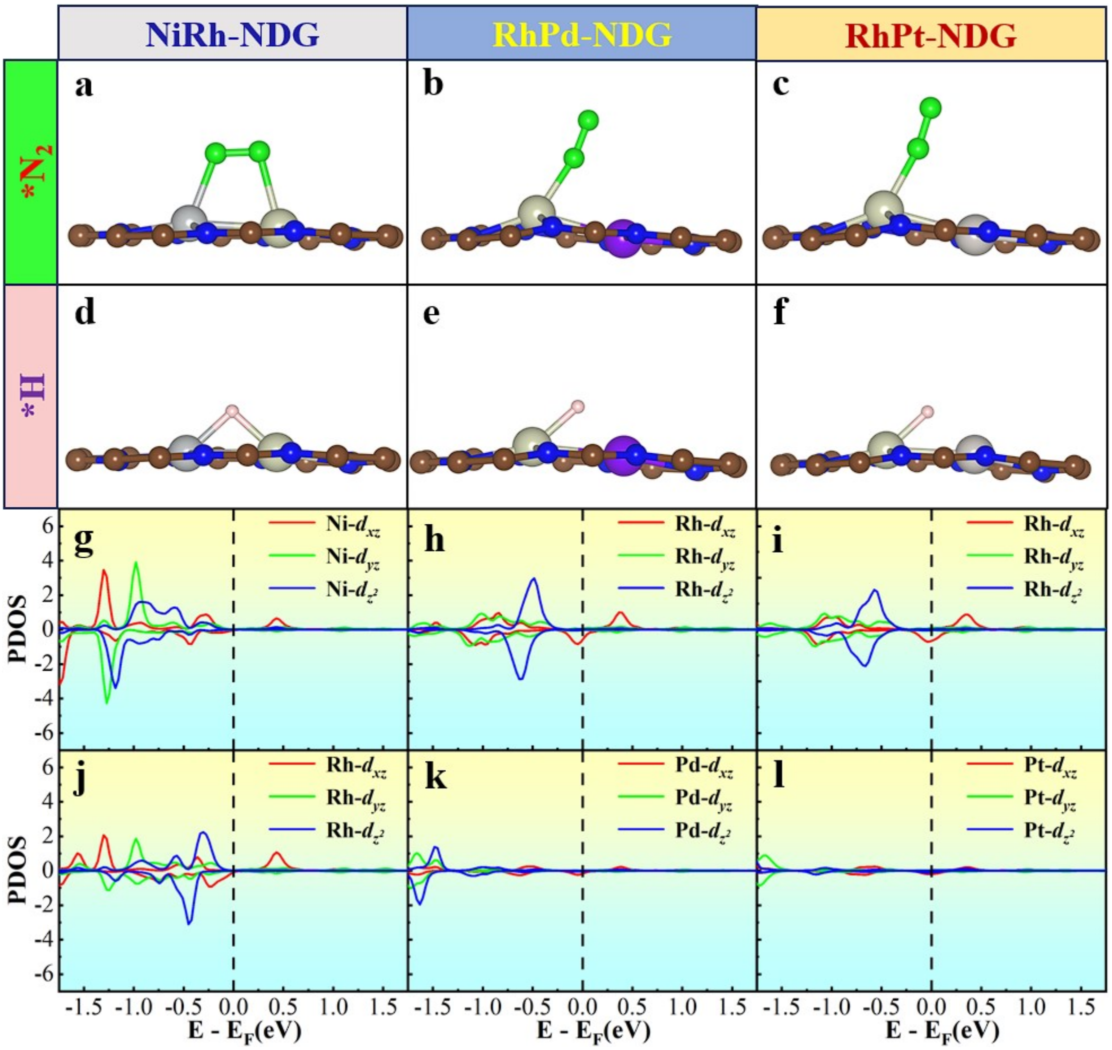

Figure S48 Front view of a. NiRh-NDG&N_2, b. RhPd-NDG&N_2, and c. RhPt-NDG&N_2; d. NiRh-NDG&H, e. RhPd-NDG&H, and f. RhPt-NDG&H; the d_{xz}, d_{yz}, d_{z^2} orbital DOS near Fermi level of M_1 atom in g. NiRh-NDG, h. RhPd-NDG, and i. RhPt-NDG; the d_{xz}, d_{yz}, d_{z^2} orbital DOS near the Fermi level of M_2 atom in j. NiRh-NDG, k. RhPd-NDG, and l. RhPt-NDG (Green atom indicate nitrogen atom in N_2).

In the study of He et al.[17], the *d* orbital of Fe_2@PDA-ZIF-900 has a significant electron distribution near the Fermi level, and thus O_2 is more inclined to take the Side-on mode when adsorbed on the surface of Fe_2@PDA-ZIF-900. Moreover, we also observed the O_2 on Fe_2@PDA-ZIF-900 was well activated by the injection of a large number of electrons, and thus the energy barrier for its $*O_2$ activation during the ORR process was drastically reduced, which are very similar to the CoCo-NDG case in our study. On the other hand, the PtFe-DAC of Bai et al.[18] corresponds to our CoPt-NDG results, where the Pt atom does not participate in bonding and only the Fe atom exchange electrons with O_2, resulting in an End-on mode. Among them, both CoPt-NDG and PtFe-DAC can utilize platinum atoms to induce the downward shift of the antibonding orbitals of the Co-O and Fe-O bonds at *OH, thus obtaining lower energy barriers for *OH desorption.

From the above results, our mechanism well explains the genesis of the adsorption modes of $*N_2$ in NRR and *H in HER, and can correspond to the experimental results, thus promising further generalized in more catalytic reactions and DACs systems.

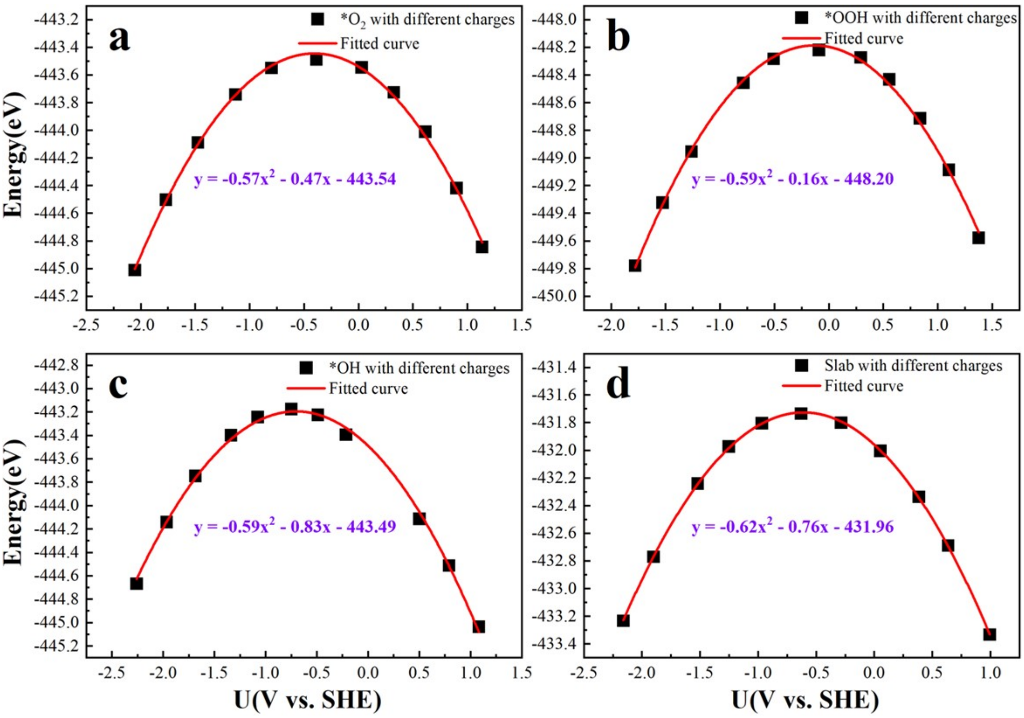

Figure S49 a. CoCo-NDG&O_2, b. CoCo-NDG&OOH, c. CoCo-NDG&OH, and d. CoCo-NDG&Slab fitted energy functional at different extra charge states.

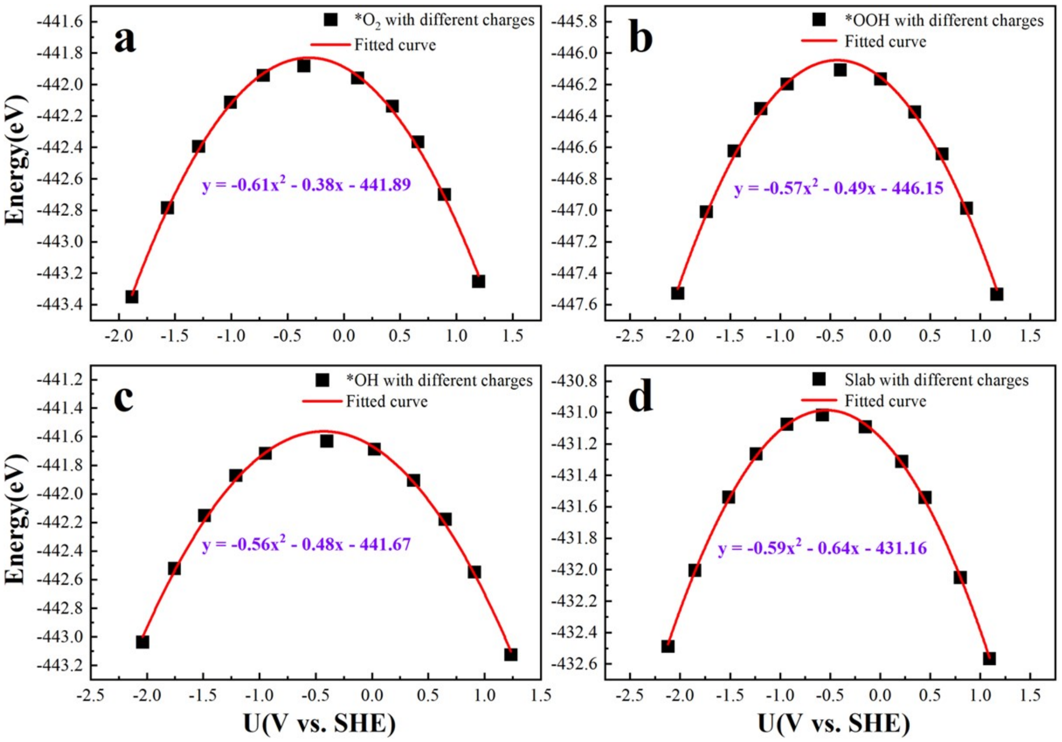

Figure S50 a. CoPt-NDG&O_2, b. CoPt-NDG&OOH, c. CoPt-NDG&OH, and d. CoPt-NDG&Slab fitted energy functional at different extra charge states.

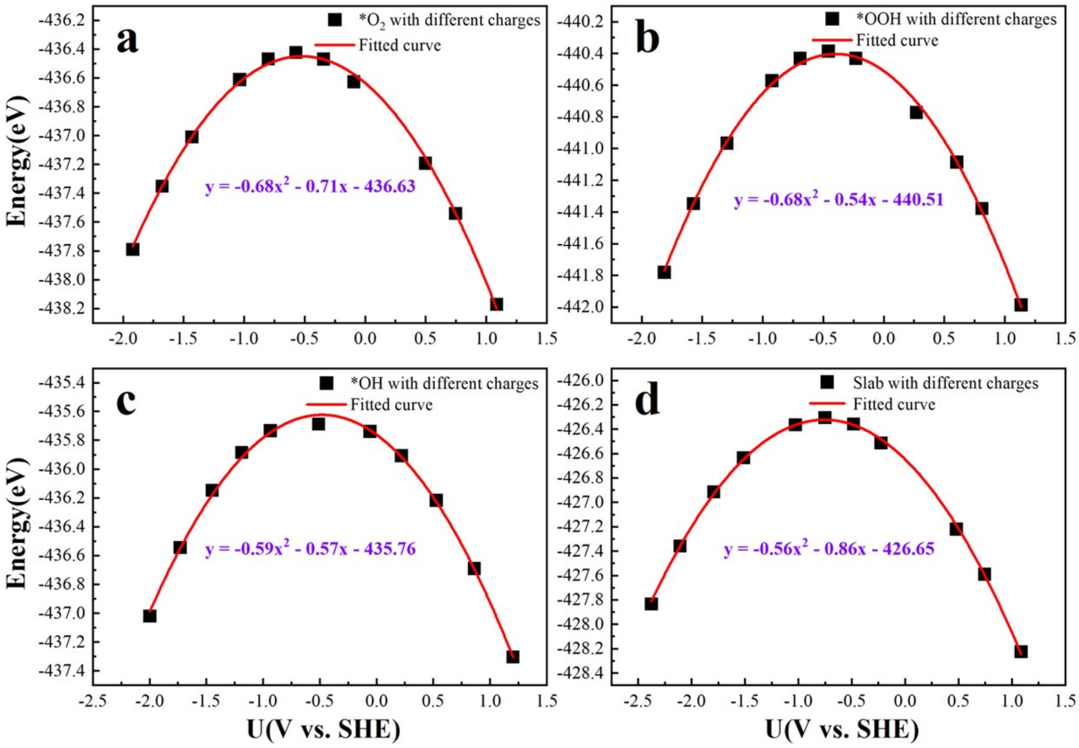

Figure S51 a. PtAu-NDG&O_2, b. PtAu-NDG&OOH, c. PtAu-NDG&OH, and d. PtAu-NDG&Slab fitted energy functional at different extra charge states.

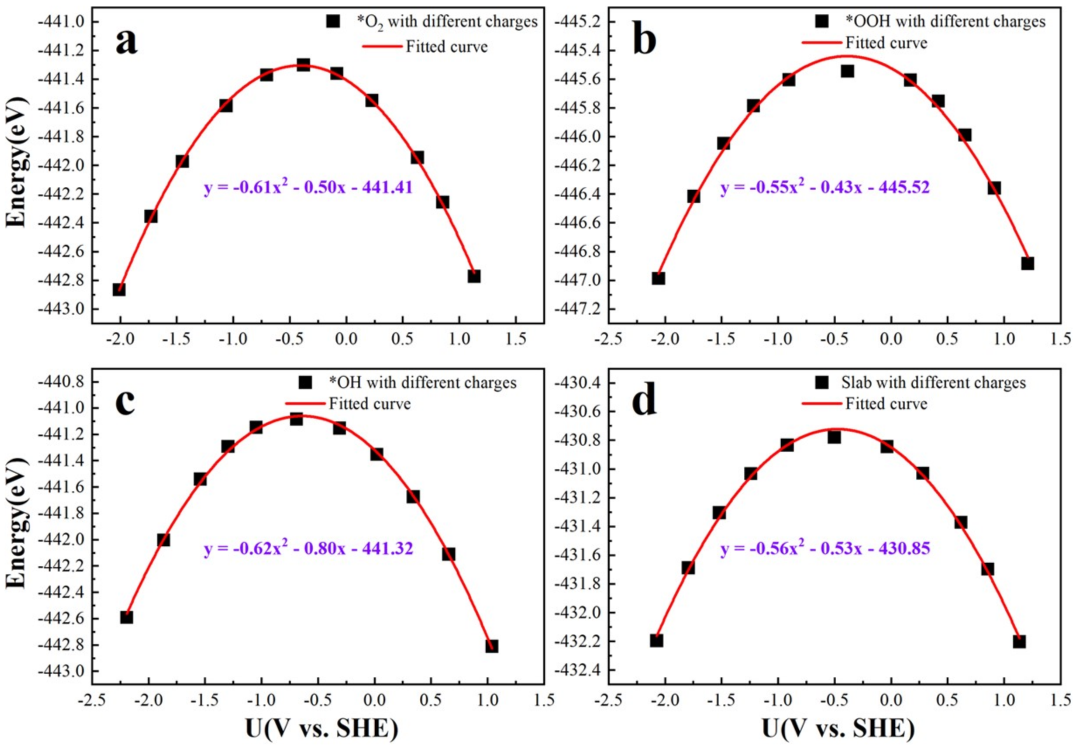

Figure S52 a. NiRh-NDG&O_2, b. NiRh-NDG&OOH, c. NiRh-NDG&OH, and d. NiRh-NDG&Slab fitted energy functional at different extra charge states.

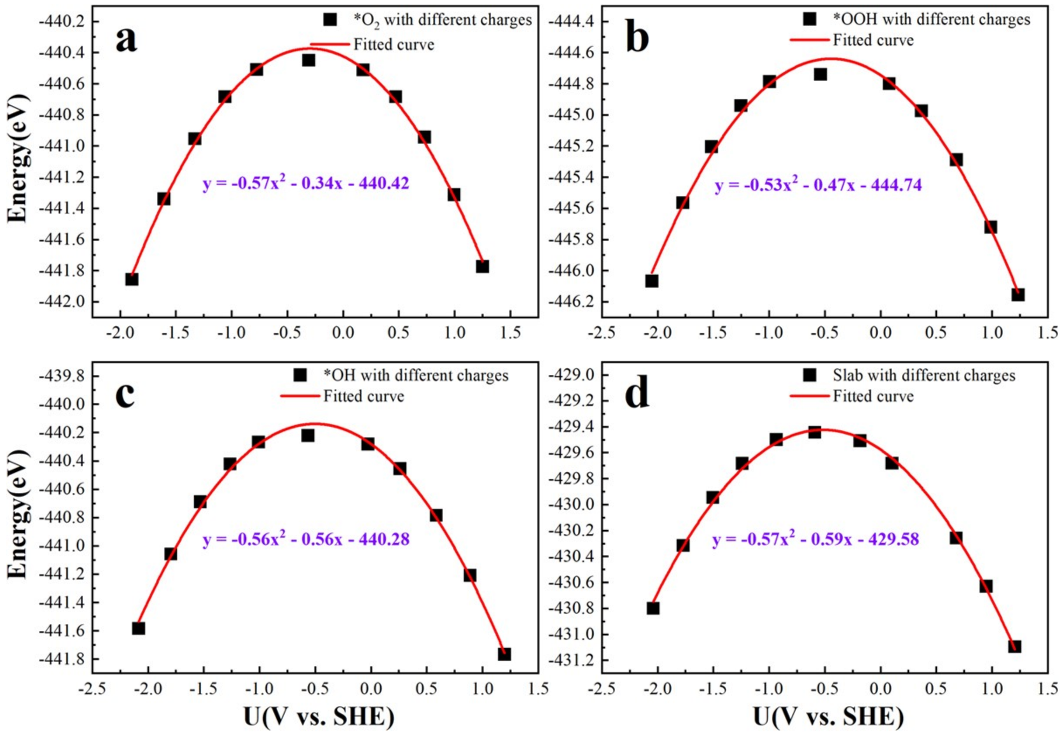

Figure S53 a. RhPd-NDG&O_2, b. RhPd-NDG&OOH, c. RhPd-NDG&OH, and d. RhPd-NDG&Slab fitted energy functional at different extra charge states.

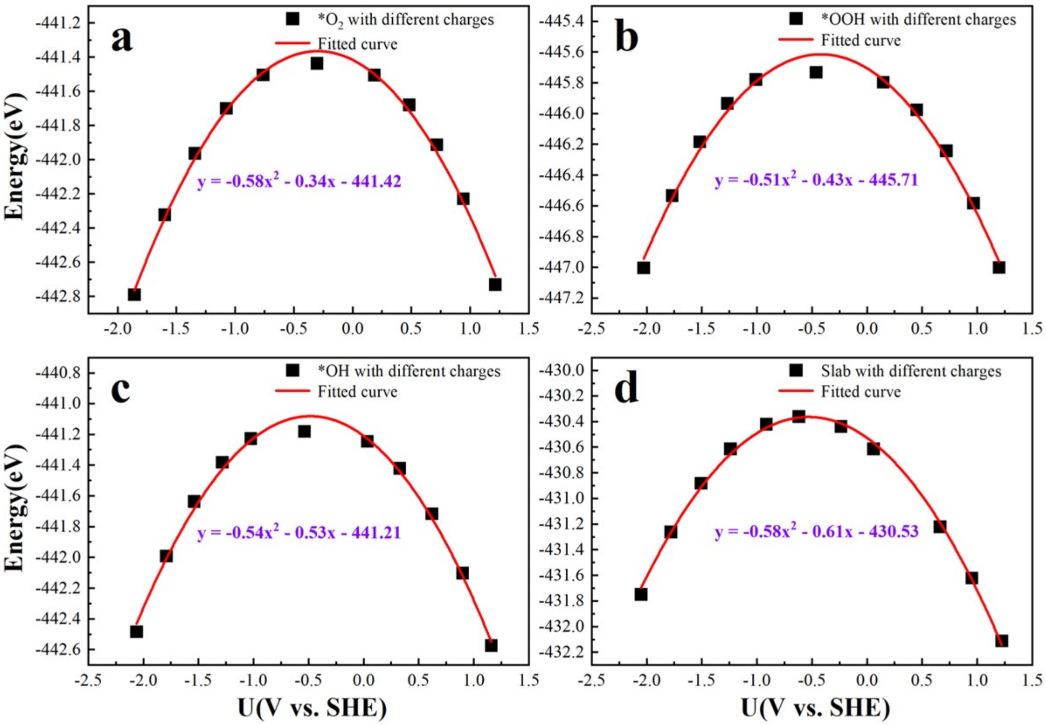

Figure S54 a. RhPt-NDG&O_2, b. RhPt-NDG&OOH, c. RhPt-NDG&OH, and d. RhPt-NDG&Slab fitted energy functional at different extra charge states.

Table S1~S7

Table S1 Types, selection ranges, step, optimal values of hyperparameter for CGCNN regression models in M_1M_2 coordination mode (learning_rate denotes the learning rate; batch_size denotes the input batch size; atom_fea_len denotes the length of the atom features; n_conv denotes number of convolutional layers; h_fea_len denotes the length of the hidden features after pooling; n_h denotes the number of hidden layers after pooling)

Model parameter	Selection Range	Step	Optimal value
learning_rate	[1e-7,1e-1]	log	0.000413
batch_size	[32,128]	32	32
atom_fea_len	[32,128]	16	32
n_con	[1,5]	1	3
h_fea_len	[32,128]	16	128
n_h	[1,5]	1	2

Table S2 Types, selection ranges, step, optimal values of hyperparameter for CGCNN regression models in M_1M_2-N_6 coordination mode

Model parameter	Range	Step	Optimal value
learning_rate	[1e-7,1e-1]	log	0.000278
batch_size	[32,128]	32	32
atom_fea_len	[32,128]	112	112
num_con_layer	[1,5]	2	2
h_fea_len	[32,128]	48	48
num_h _layer	[1,5]	1	1

Table S3 Types, selection ranges, step, optimal values of hyperparameter for CGCNN regression models in M_1M_2-N_6-C coordination mode

Model parameter	Range	Step	Optimal value
learning_rate	[1e-7,1e-1]	log	0.000189
batch_size	[32,128]	32	32
atom_fea_len	[32,128]	16	80
num_con_layer	[1,5]	1	3
h_fea_len	[32,128]	16	128
num_h _layer	[1,5]	1	1

Table S4 Types, selection ranges, step, optimal values of hyperparameter for CGCNN regression models in M_1M_2-NDG coordination mode

Model parameter	Range	Step	Optimal value
learning_rate	[1e-7,1e-1]	log	0.011068
batch_size	[32,128]	96	32
atom_fea_len	[32,128]	128	80
num_con_layer	[1,5]	5	3
h_fea_len	[32,128]	112	128
num_h _layer	[1,5]	1	1

Table S5 Free energy barrier of ORR for Pt/C catalyst (The reaction energy barrier of the PDS have been marked in red)

Step	**Reaction energy barrier (eV)**
Slab → $*O_2$	-0.77
$*O_2$ → *OOH	0.97
*OOH → *O	-0.32
*O → *OH	-0.15
*OH → Slab	0.27

TableS6 ORR overpotential calculated by DFT ($\eta_{ORR, DFT}$) vs. ORR potential predicted by ML and predicted value ($\eta_{ORR, ML}$) of 22 DACs obtained after Stability, Selectivity, ORR activity screening.

DACs	$\eta_{ORR, DFT}$ **(V)**	$\eta_{ORR, ML}$ **(V)**
NiPd-NDG	0.97	0.89
CoAu-NDG	0.95	1.04
CuPt-NDG	0.91	0.98
CuZn-NDG	0.90	1.09
RhAu-NDG	0.90	1.02
CuCu-NDG	0.89	0.84
CuPd-NDG	0.88	1.06
NiCu-NDG	0.87	0.97
CoCu-NDG	0.87	1.01
CuRh-NDG	0.87	1.04
AgPt-NDG	0.86	1.07
CuAg-NDG	0.85	1.03
NiAg-NDG	0.83	1.10
RhPd-NDG	0.83	1.05
ZnAu-NDG	0.81	0.93
CoAg-NDG	0.81	0.98
CoPd-NDG	0.81	0.87
NiRh-NDG	0.80	0.89
CuIr-NDG	0.79	1.07
RhPt-NDG	0.77	0.95
NiIr-NDG	0.73	0.85
CoPt-NDG	0.69	0.88

Table S7 Evaluation results of CGCNN regression model with different coordination modes on tagged dataset.

	M_1M_2	M_1M_2-N6	M_1M_2-N6-C	M_1M_2-NDG
MAE_{Avg}	0.249	0.188	0.133	0.239
MAE_{min}	0.216	0.163	0.119	0.210
MAE_{Max}	0.282	0.215	0.146	0.275
$RMSE_{Avg}$	0.388	0.276	0.216	0.348
$RMSE_{Min}$	0.301	0.232	0.192	0.288
$RMSE_{Max}$	0.436	0.312	0.237	0.402
R^2_{Avg}	0.865	0.931	0.957	0.890
R^2_{Min}	0.820	0.909	0.943	0.842
R^2_{Max}	0.909	0.947	0.968	0.920

References

(1) Nørskov, J. K.; Rossmeisl, J.; Logadottir, A.; Lindqvist, L. R. K. J.; Kitchin, J. R.; Bligaard, T.; & Jonsson, H. Origin of the overpotential for oxygen reduction at a fuel-cell cathode. *J. Phys. Chem. B* **2004**, *108* (46), 17886-17892.

(2) Guo, X.; Gu, J.; Lin, S.; Zhang, S.; Chen, Z.; Huang, S. Tackling the Activity and Selectivity Challenges of Electrocatalysts toward the Nitrogen Reduction Reaction via Atomically Dispersed Biatom Catalysts. *J. Am. Chem. Soc.* **2020**, *142*, 5709–5721.

(3) Mathew, K.; Sundararaman, R.; Letchworth-Weaver, K.; Arias, T.A. Implicit solvation model for density-functional study of nanocrystal surfaces and reaction pathways. Hennig, R.G. *J. Chem. Phys.* **2014**, *140*(8), 084106.

(4) Hagopian, A.; Doublet, M.-L.; Filhol, J.-S.; Binninger, T. Advancement of the homogeneous background method for the computational simulation of electrochemical interfaces. *J. Chem. Theory Comput.* **2022**, *18* (3), 1883−1893.

(5) Mathew, K.; Kolluru, V.; Mula, S.; Steinmann, S. N.; Hennig, R. G. Implicit self-consistent electrolyte model in plane-wave density functional theory. *J. Chem. Phys.* **2019**, *151*, 234101.

(6) Verma, A. M.; Laverdure, L.; Melander, M. M.; & Honkala, K. Mechanistic origins of the pH dependency in Au-catalyzed glycerol electro-oxidation: insight from first-principles calculations. *ACS Catal.* **2021**, *12* (1), 662-675.

(7) Liu, J.-C.; Luo, F.; Li, J. Electrochemical Potential-Driven Shift of Frontier Orbitals in M–N–C Single-Atom Catalysts Leading to Inverted Adsorption Energies. *J. Am. Chem. Soc.* **2023**, *145* (46): 25264-25273.

(8) Deringer, V. L.; Tchougréeff, A. L. Crystal orbital Hamilton population (COHP) analysis as projected from plane-wave basis sets. *J. Phys. Chem.* **2011**, *115*, 5461-5466.

(9) Nelson, R.; Ertural, C.; George, J.; Deringer, V. L.; Hautier, G.; Dronskowski, R. LOBSTER: Local Orbital Projections, Atomic Charges, and Chemical-Bonding Analysis from Projector-Augmented-Wave-Based Density-Functional Theory. *J. Comput. Chem.* **2020**, *41*, 1931−1940.

(10) Xie, T.; Grossman, J. C. Crystal Graph Convolutional Neural Networks for an Accurate and Interpretable Prediction of Material Properties. *Phys. Rev. Lett.* **2018**, *120* (14): 145301.

(11) Chen, C.; Ye, W.; Zuo, Y.; Zheng, C.; Ong, S. P. Graph Networks as a Universal Machine Learning Framework for Molecules and Crystals. *Chem. Mater.* **2019**, *31* (9),3564–3572.

(12) Pedregosa, F.; Varoquaux, G.; Gramfort, A.; Michel, V.; Thirion, B.; Grisel, O.; Blondel, M.; Prettenhofer, P.; Weiss, R.; Dubourg, V.; Vanderplas, J.; Passos, A.; Cournapeau, D.; Brucher, M.; Perrot, M.; Duchesnay, E. Scikit-Learn: Machine Learning in Python. *J. Mach. Learn. Res.* **2011**. *12*, 2825-2830.

(13) Lam Pham, T.; Kino, H.; Terakura, K.; Miyake, T.; Tsuda, K.; Takigawa, I.; Chi Dam, H. Machine Learning Reveals Orbital Interaction in Materials. *Sci. Technol. Adv. Mater.* **2017**, *18* (1), 756-765.

(14) Liu, K.; Fu, J.; Lin, Y.; Luo, T.; Ni, G.; Li, H.; Lin, Z.; Liu, M. Insights into the Activity of

Single-Atom Fe-N-C Catalysts for Oxygen Reduction Reaction. *Nat. Commun.* **2022**, *13* (1), 2075.

(15) Peterson, A. A.; Abild-Pedersen, F.; Studt, F.; Rossmeisl, J.; & Nørskov, J. K. How copper catalyzes the electroreduction of carbon dioxide into hydrocarbon fuels. *Energy Environ. Sci.* **2010**, *3*(9), 1311-1315.

(16) Su, H.; Song, S.; Li, N.; Gao, Y.; Li, P.; Ge, L.; Ma, T. Flexibility Tuning of Dual-Metal S-Fe- Co- N5 Catalysts with O-Axial Ligand Structure for Electrocatalytic Water Splitting. *Adv. Energy Mater.* **2023**, *13*(41), 2301547.

(17) Leng, K.; Zhang, J.; Wang, Y.; Li, D.; Bai, L.; Shi, J.; Qu, Y. Interfacial Cladding Engineering Suppresses Atomic Thermal Migration to Fabricate Well-Defined Dual-Atom Electrocatalysts. *Adv. Funct. Mater.* **2022**, *32*(41), 2205637.

(18) Zhang, Z.; Dai, Y.; Guo, P.; Liu, B.; Xia, Y.; Tu, F.; Wang, Z. Noncovalent Assembly Strategy for Efficient Synthesis of Dual-Atom Catalysts. *Adv. Funct. Mater.* **2024**, 2407128.